UNSTEADY AERODYNAMICS OF CAMBERED AIRFOILS AT LOW REYNOLDS NUMBER

A THESIS SUBMITTED TO
THE GRADUATE SCHOOL OF NATURAL AND APPLIED SCIENCES
OF
MIDDLE EAST TECHNICAL UNIVERSITY

BY

TAWFIQ AHMED

IN PARTIAL FULFILLMENT OF THE REQUIREMENTS
FOR
THE DEGREE OF MASTER OF SCIENCE
IN
AEROSPACE ENGINEERING

FEBRUARY 2022

Approval of the thesis:

UNSTEADY AERODYNAMICS OF CAMBERED AIRFOILS AT LOW REYNOLDS NUMBER

submitted by **TAWFIQ AHMED** in partial fulfillment of the requirements for the degree of **Master of Science in Aerospace Engineering, Middle East Technical University** by,

Prof. Dr. Halil Kalıpçılar
Dean, Graduate School of **Natural and Applied Sciences** _____

Prof. Dr. Serkan Özgen
Head of the Department, **Aerospace Engineering, METU** _____

Prof. Dr. Dilek Funda Kurtuluş
Supervisor, **Aerospace Engineering, METU** _____

Examining Committee Members:

Prof. Dr. Sinan Eyi
Aerospace Engineering, METU _____

Prof. Dr. Dilek Funda Kurtuluş
Aerospace Engineering, METU _____

Assoc. Prof. Dr. Nilay Sezer Uzol
Aerospace Engineering, METU _____

Assist. Prof. Dr. Özge Başkan Perçin
Aerospace Engineering, METU _____

Assist. Prof. Dr. Mustafa Kaya
Aerospace Engineering, AYBÜ _____

Date: 08.02.2022

I hereby declare that all information in this document has been obtained and presented in accordance with academic rules and ethical conduct. I also declare that, as required by these rules and conduct, I have fully cited and referenced all material and results that are not original to this work.

Name, Last name: Tawfiq Ahmed

Signature:

ABSTRACT

UNSTEADY AERODYNAMICS OF CAMBERED AIRFOILS AT LOW REYNOLDS NUMBER

Ahmed, Tawfiq
Master of Science, Aerospace Engineering
Supervisor: Prof. Dr. Dilek Funda Kurtuluş

February 2022, 81 pages

Almost all the insects and birds fly at very low Reynolds numbers. Therefore, to design micro air vehicles (MAVs), a study of airfoils and wings at low Reynolds numbers is essential. Unsteady flow behavior at low Reynolds numbers can vary for different airfoils depending on their camber, maximum thickness, or maximum camber position. Numerical simulations of cambered airfoils (NACA 1412, NACA 2412, NACA 3412, NACA 4412) at Re = 1000 are conducted in the current study to understand the camber effect on the unsteady aerodynamic behavior at a low Reynolds number. The numerical simulations are performed at angles of attack ranging from 0° to 10° with an increment of 1°. A domain with a C-type shape for upstream flow and a rectangular shape for downstream flow is prepared for meshing. Meshes are generated using both a structured grid in the outer region and an unstructured grid in the inner region. Thick boundary layers are implemented around airfoils as at low Reynolds numbers boundary layer gets thicker. The aerodynamic coefficients, pressure distributions, flow separations, and wake flow fields are

analyzed from the simulations in detail in the two-dimensional domain. The airfoil producing the highest lift is then simulated in the three-dimensional domain to compare the data with the 2D simulation. In each chapter, the effects of camber are discussed with results.

Keywords: Flapping wing, unsteady aerodynamics, Micro Air Vehicles, low Reynolds number, Computational Fluid Dynamics, cambered airfoils.

ÖZ

DÜŞÜK REYNOLDS SAYILARINDA KAMBURLU KANAT PROFİLLERİNİN ZAMANA BAĞLI AERODİNAMİĞİ.

Ahmed, Tawfiq
Yüksek Lisans, Havacılık ve Uzay Mühendisliği
Tez Yöneticisi: Prof. Dr. Dilek Funda Kurtuluş

Şubat 2022, 81 sayfa

Neredeyse tüm böcekler ve kuşlar çok düşük Reynolds sayılarında uçarlar. Bu nedenle, mikro hava araçları (MAV'ler) tasarlamak için, düşük Reynolds sayılarında kanat profilleri ve kanatların incelenmesi esastır. Düşük Reynolds sayılarında durağan olmayan akış davranışı, farklı kanat profilleri için eğimlerine, maksimum kalınlıklarına veya maksimum eğim konumlarına bağlı olarak değişebilir. Mevcut çalışmada, düşük Reynolds sayısında kararsız aerodinamik davranış üzerindeki kambur etkisini anlamak için Re = 1000'de kamburlu kanat profillerinin (NACA 1412, NACA 2412, NACA 3412, NACA 4412) sayısal simülasyonları yapılmıştır. Sayısal simülasamburyonlar, 1°'lik artışlarla 0° ila 10° arasında değişen hücum açılarında gerçekleştirilir. Ağ oluşturma için, yukarı akış için C tipi bir şekle ve aşağı akış için dikdörtgen bir şekle sahibomp bir alan hazırlanır. Ağlar, hem dış bölgede yapılandırılmış bir ızgara hem de iç bölgede yapılandırılmamış bir ızgara kullanılarak oluşturulur. Düşük Reynolds sayılarında sınır tabakası kalınlaştığı için

kanat profillerinin etrafına kalın sınır tabakaları uygulanır. Aerodinamik katsayılar, basınç dağılımları, akış ayrımları ve iz akış alanları, iki boyutlu alanda simülasyonlardan ayrıntılı olarak analiz edilir. En yüksek kaldırmayı üreten kanat profili daha sonra verileri iki boyutlu simülasyonla karşılaştırmak için üç boyutlu alanda simüle edilir. Her bölümde kamberin etkileri sonuçlarla tartışılmıştır.

Anahtar Kelimeler: Çırpınan kanat, kararsız aerodinamik, Mikro Hava Araçları, düşük Reynolds sayısı, Hesaplamalı Akışkanlar Dinamiği, kamburlu kanat profilleri.

To my family whose support always encouraged me,

To my friends who were always there for me.

ACKNOWLEDGMENTS

I would like to express my gratitude to my thesis advisor Prof. Dr. Dilek Funda Kurtuluş for her guidance and inspiration throughout my thesis. She was always supportive and helpful in every phase of my thesis work. Without her, I could not have achieved this much skill and knowledge.

I owe my deepest regard to my father Mahbub Hossain Kutial, to my mother Sofura Begum, and to my sister Tofa Ahmed for supporting me not only when I was facing a tough time while working on my thesis but also every critical decision I had to take to come to this position.

I would like to thank my friends and lab partners Özgün Çalış, Altuga Ökmen, Mürvet Bektaş, Berkan Anılır for their help, friendship, and always staying with me through this thesis process.

Finally, I want to thank UHEM (National Center for High Performance Computing) for helping me to use their High Performance Computing (HPC) facility which was a great help for my analyses.

Computing resources used in this work were provided by the National Center for High Performance Computing of Turkey (UHeM) under grant number 4011302021.

TABLE OF CONTENTS

LIST OF TABLES

TABLES

LIST OF FIGURES

FIGURES

CHAPTER 1

INTRODUCTION

Humankind has always been fascinated by flying like birds and throughout history, there have been numerous attempts to build a flying machine that can fly like birds. Since the time of Leonardo da Vinci's conceptualized design of flying machines to this date, the progress in the aerospace industry is tremendous. Most of these developments are encouraged and financed to support the need in military operations and civil air transportation. Typical aircrafts used in these sectors are big enough to capacitate human passengers onboard and need long take-off and landing airstrips. Rapid progress in aircraft technology led to Unmanned Aerial Vehicle (UAV) that can be operated remotely and are used for military surveillance, military operations, or civil uses like mapping, surveying lands, and delivering cargoes. The purpose of inventing flapping-wing micro air vehicles (FWMAVs) is to make small and compact designs of aircraft that can be used in applications like surveillance on the battlefield and hazardous environments similar to unmanned air vehicles (UAVs) (L.-J. Yang & Esakki, 2021).

These flapping wing MAVs also have the potential to be used in Search and Rescue (SAR) missions, environmental surveillance, and first-aid crews (Altenbuchner & Hubbar Jr, 2018).

MAVs can be defined as flying vehicles having a dimension less than 15 cm however future MAVs may be as small as common insects (Platzer & Jones, 2006). Because of the advantage of aerodynamic efficiency of flapping-wing MAVs in this flight regime, research and development efforts are mostly focused on MAVs (Bohorquez et al., 2010). Flapping wing aerial vehicles fall in the Small Unmanned Aerial Vehicles (SUAVs) category that combines the ability to hover like rotary-wing aircraft (like hummingbirds), while also allowing gliding flight capacity like fixed-wing aircraft (Thomas & Boyer, 2011). Flapping wing vehicles have the ability to

dive and perch, are tremendously maneuverable and agile, and have enhanced safety and reduced noise emissions when compared to rotary-wing vehicles.

On top of that, flapping-wing vehicles have visual characteristics, which makes them ideal for contextual camouflage (Altenbuchner & Hubbar Jr, 2018). wing vehicles are able to integrate three sides of the performance triangle: (1) ideal performance at low Reynolds number flight regime, (2) agility and maneuverability, and (3) mission adaptability in one vehicle, as in Figure 1. Thus, FWMAVs fill in the gap in the design space in SUAV's (Grauer & Hubbard, 2011).

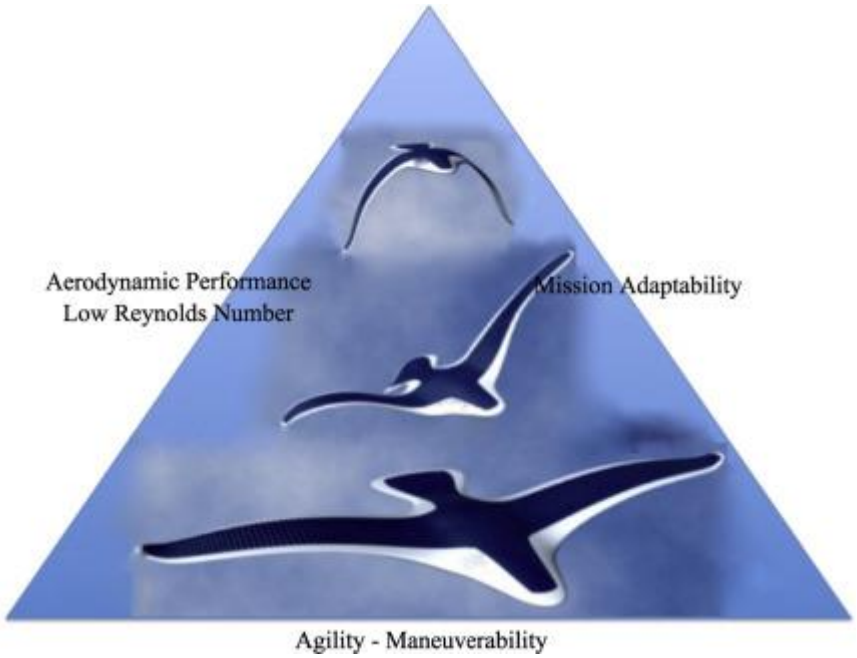

Figure 1: Flapping wing vehicle capabilities (NASA Langley., 2014).

There are almost a million species of insects, and non-insects, another 13,000 warm-blooded vertebrate species (including mammals, about 9,000 species of birds, and 1,000 species of bats) that can fly in the skies. Birds, bats, and insects have nature's finest locomotive ability to maneuver their bodies effectively in the air. Technology in the aeronautical field has been developing with immense speed for the last 100 years whereas these species are evolved for over 150 million years and are still impressive (Shyy, 2008).

Figure 2: Bumblebee flights even when the wing to body ratio is incredibly small (Unsplash, 2021).

In terms of top speed, humans move at top speeds of 3-4 body lengths per second, a racehorse runs approximately 7 body lengths per second, a cheetah can run 18 body lengths per second (Norberg, 1990), and a supersonic aircraft (like SR-71

Figure 3: Flights of birds while gliding with big wings (Unsplash, 2021).

“Blackbird”) flying at Mach 3 which is about 900 m/s cover around 32 body lengths per second, whereas a common Pigeon (Columba livia) can cover about 75 body lengths per second at a speed of 22.4 m/s. Some faster birds like a European Starling (Sturnus vulgaris) can cross 120 body lengths per second, some other species of swift can even cover 140 body lengths per second (McMasters & Henderson, 1980).

In flapping-wing vehicle design, wing design is the most important aspect as in flapping-wing vehicles both lift and thrust are generated only by the wing which is unlike the design methodology of conventional fixed-wing or rotary-wing aircraft. A design of a flapping wing vehicle, the Dove is shown in Figure 4 (W. Yang et al., 2018).

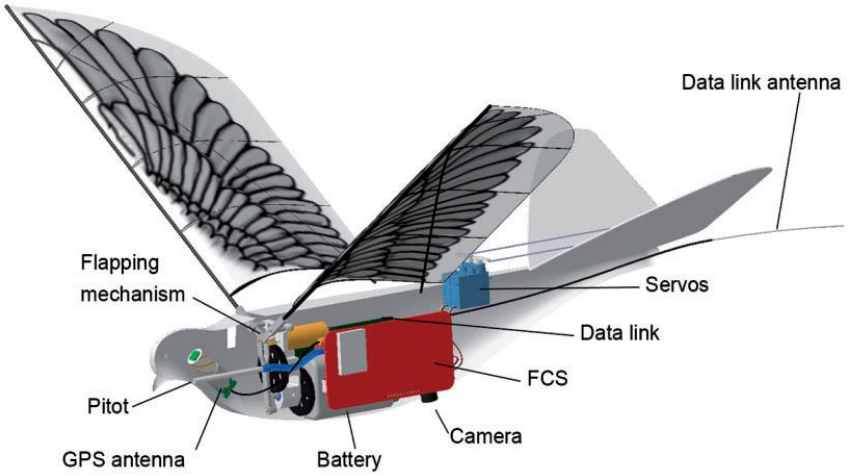

Figure 4: Configuration of the Dove.

However, building MAVs is not an easy task to perform as existing theories only cover unsteady aerodynamics beyond the steady, stationary wing theories (C. K. Kang & Shyy, 2013). Especially, clap and fling (Weis-Fogh, 1973), delayed stall via prolonged leading-edge vortices (LEVs) (Ellington et al., 1996) wake-capture of a wing during the return stroke (Birch & Dickinson, 2003; Dickinson et al., 1999), and rotational forces due to combined pitching and plunging (Dickinson et al., 1999; Sane & Dickinson, 2002) allow valuable information about insects’ flight mechanics and aerodynamics. These insights of unsteady physical processes are extremely important to understand the flapping mechanism of small flyers like fruit flies, that flies at a Reynolds number $Re = Uc/\upsilon$ is around 102 where, U is the midstroke

velocity, c is the wing chord length, and υ is the kinematic viscosity (C. K. Kang & Shyy, 2013).

A recent mission to Mars by NASA included a rotorcraft that was specially designed for Mars atmosphere. However, flying on Mars stays challenging as the atmospheric density of Mars is ultra-thin (1.3% of the air density on Earth) and the gravitational acceleration on Mars is 38% of Earth's 9.8 m/s2 (C. Kang et al., 2018). In order to design a flying vehicle that can fly on Mars, that flying vehicle should be able to operate in unsteady aerodynamic conditions with low Reynolds number and with a high lift coefficient just like the insects fly on Earth (Shyy et al., 2013). This is how the concept of Marsbee design was introduced (Bluman & Kang, 2017).

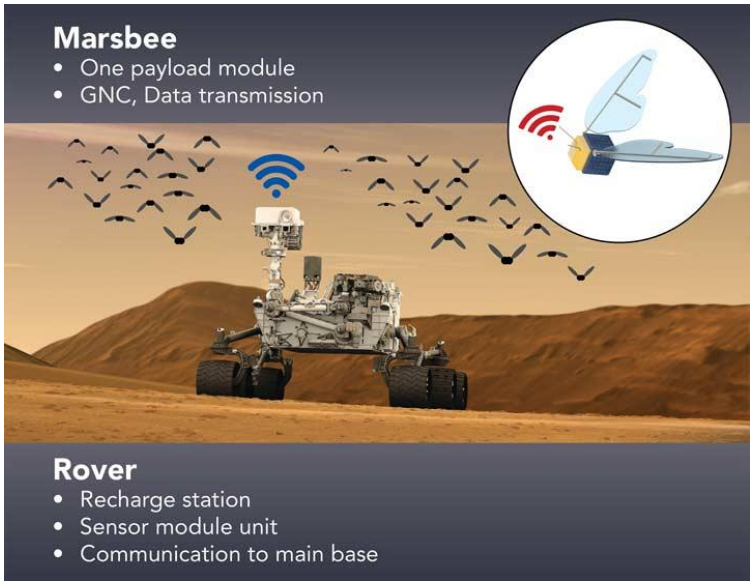

Figure 5: Marsbee on Mars (a concept design).

Low speed and small length scales of insects and birds allow them to fly at a flight regime of Reynolds number 10^3-10^4 and 10^4-10^5 respectively (Shyy, 2008). Birds like hummingbirds fly at Re = O (10^4), on the other hand, small insects (fruit-flies, honeybees) fly at Re = O (10^2 – 10^3) (C. K. Kang & Shyy, 2013) A mechanism like flapping wing MAVs needs a more favorable wing design for low Reynolds numbers in order to imitate the flights of birds and insects than fixed-wing MAVs. Thus,

studies in this low Reynolds number flight regime are necessary for available airfoil wing profiles.

Figure 6: Flapping flight mode of Hummingbird(Unsplash, 2021).

To enhance the understanding of vortex shedding patterns, unsteady aerodynamics behavior of flapping wings at low Reynolds number with the steady outer condition is necessary. Most of the time, these flight models for flapping motions are based on quasi-steady approaches (Kurtulus, 2015). Fundamental knowledge on the properties of the flapping wing in the steady condition is also valuable to understand the properties of the same wing in unsteady conditions. To understand perching and flapping airfoils, Cl- α, Cl-Cd relations on the effective angle of attack are useful (Platzer & Jones, 2006).

Experimental and numerical studies on vortex formation were conducted by Ohmi et al. (Ohmi et al., n.d.) on an ellipse as well as on a NACA 0012 airfoil at Reynolds number starting from 1500 up to 10000. All the experiments were conducted in a tank full of water and the flow wake characteristics were categorized as per the development of shedding vortices, synchronized shedding type, parallel shedding type, and vortex superposition type. Kurtulus et al. (Kurtulus, 2015) experimented using the same methodology but with a modified mechanism to investigate flow behavior around NACA 0012 airfoil at Re =1000 for pitching and plunging motions.

Recently, perching maneuvers of flapping wings at low Reynolds numbers have gained some interest. The perching maneuver is like a pitch-up motion when the wing faces a large change of angle of attack. A previous study was conducted by Ol

et al. (Ol et al., 2009) to investigate the flow pattern around flat plate and ellipse with a thickness of 10% at a constant pitch rate at Re = 100, and Re = 1000 at angles of attack ranging from 0° to 40°. To control MAVs and model the mechanism models, the knowledge of the flow physics around micro air vehicles at steady conditions will contribute a lot especially in cases with response behavior against gusts, perching motion, flight maneuvers, and flapping motions.

The knowledge of the physics of flow separation and vortex formation is valuable because even at steady external conditions, wakes behind airfoils and bluff bodies at high angles of attack are unsteady (Gopinath & Jameson, 2006). As at low Reynolds number flow is laminar, a mild adverse pressure gradient can cause separation to the flow.

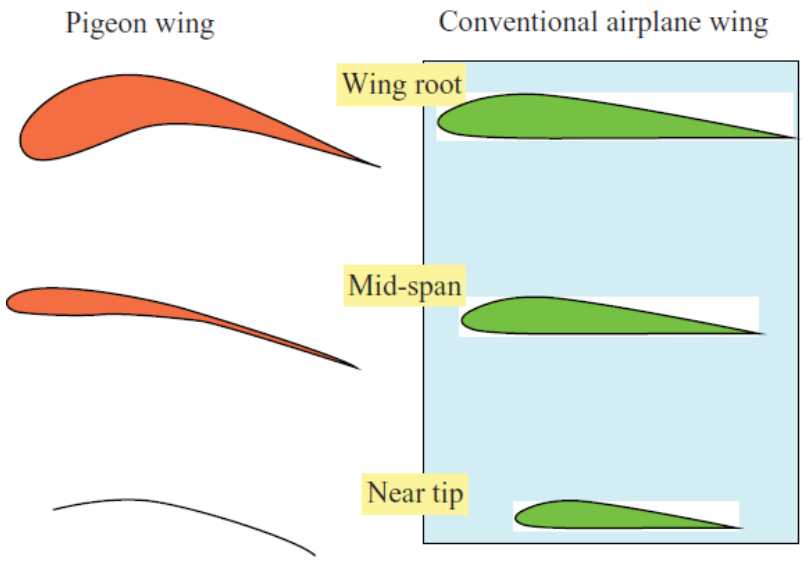

Figure 7: Wing cross-section comparison between a pigeon wing and a conventional transport airplane wing. Pigeon wing cross section shows significantly difference spanwise in terms of camber and thickness (Shyy et al., 2013).

Most of the studies in literature are focused on higher Reynolds number and the lack of works at very low Reynolds number flight regime is the main inspiration for this study. To give a brief idea of where this study stands in the literature, a list of

different studies at low Reynolds number (Re = 1000 to 2000) has been presented in table

Table 1: Comparison of different studies in literature at low Reynolds numbers for different cambered airfoils.

Re	Airfoil	Camber	Thickness	Method	Reference
400	NACA 4404	0.04	0.04	Numerical	(Mateescu & Abdo, 2010)
800	NACA 4404	0.04	0.04	Numerical	(Mateescu & Abdo, 2010)
1000	NACA 0000	0.00	0.00	Numerical	(Gopalakrishnan Meena et al., 2018)
1000	NACA 0006	0.00	0.06	Numerical	(Gopalakrishnan Meena et al., 2018)
1000	NACA 0012	0.00	0.12	Numerical	(Gopalakrishnan Meena et al., 2018; Kurtulus, 2016)
1000	NACA 0018	0.00	0.18	Numerical	(Gopalakrishnan Meena et al., 2018)
1000	NACA 4402	0.04	0.02	Numerical	(P. J. Kunz, 2003)
1000	NACA 1412	0.01	0.12	Numerical	Current Study
1000	NACA 2412	0.02	0.12	Numerical	Current Study
1000	NACA 3412	0.03	0.12	Numerical	Current Study
1000	NACA 4412	0.04	0.12	Numerical	Current Study
1200	NACA 0012	0.00	0.12	Experimental	(Huang et al., 2001)
2000	NACA 0008	0.00	0.08	Numerical	(P. Kunz & Kroo, 2000)
2000	NACA 0006	0.00	0.06	Numerical	(P. Kunz & Kroo, 2000)
2000	NACA 0004	0.00	0.04	Numerical	(P. Kunz & Kroo, 2000)
2000	NACA 0002	0.00	0.02	Numerical	(P. Kunz & Kroo, 2000)

A previous study on the effect of cambered airfoils NACA 0002, and NACA 4402 for Re = 1000, Re = 2000, Re = 6000 with angles of attack ranging from 0° to 10°

has been conducted by Kunz (P. J. Kunz, 2003)and they denoted that the camber increases the maximum lift-to-drag ratio for the Reynolds number range investigated (Kunz, 2003).

A detailed study on NACA 0012 for angles of the attack starting from 0° to 90° at low Reynolds number (Re = 1000), gives a very good idea of the unsteady aerodynamics behavior of the flow around a symmetric airfoil as the angles of attack increase (Kurtulus, 2015, 2016), and the wake of the symmetric airfoil has been distinguished to performed different modes depending on the angle of attack.

The same approach has been taken into account for the current study. The unsteady aerodynamics around 4 cambered airfoils is simulated at a very low Reynolds number. Most of the studies in literature on flapping wing airfoils at low Reynolds number are symmetric airfoils. Some interesting and valuable studies have been conducted on cambered airfoils at low Reynolds number however, effective, and thorough studies on mostly used cambered airfoils: NACA 1412, NACA 2412, NACA 3412, and NACA 4412 are absent. Therefore, the main goal of this study is to provide a detailed and thorough analysis on these airfoils in order to understand the camber effect at very low Reynolds number flight regime which will benefit in future flapping wing design process.

Numerical analyses have been conducted around NACA 1412, NACA 2412, NACA 3412, and NACA 4412 for a range of angles of the attack starting from 0° to 10° at Re = 1000. Most of the insects and birds fly at a very low Reynolds number (Re = $10^3 – 10^4$) flight regime and as the purpose of this study is to observe the unsteady behavior of the cambered airfoils at those Reynolds number range, so Re = 1000 has been used for this study. The simulations are conducted by using the commercial software ANSYS Fluent.

CHAPTER 2

SIMULATION METHODOLOGY

2.1 Equations and Domain Geometry

Navier-Stokes equations have been used for the calculations and the equations for laminar, incompressible, and 3D flow are given in Eq. 1 and Eq. 2:

$$\vec{\nabla}.\vec{V} = 0 \tag{1}$$

$$\frac{\partial \vec{V}}{\partial t} + \left(\vec{\nabla}.\vec{V}\right)\vec{V} = -\frac{1}{\rho}\vec{\nabla}p + \upsilon\nabla^2\vec{V} \tag{2}$$

where, the velocity is $\vec{V}$, the fluid density is ρ, the pressure is p, and the kinematic viscosity is υ.

ANSYS Fluent uses the finite-volume method for simulation (ANSYS Fluent Users Guide). During the analysis, the second-order implicit method has been used for the transient solution. The SIMPLE-type implicit algorithm is implemented for pressure-velocity coupling. SIMPLE algorithm is used for solving Navier-Stokes equations and it stands for Semi-Implicit Method for Pressure Linked Equations. Solving a steady-state problem by iteration process does not resolve problems in terms of pressure-velocity coupling as changes are not small in consecutive solutions. So, SIMPLE algorithm solves the momentum equation and gives an approximation of the velocity field. Then, using an initial guess or from previous iteration pressure gradient term is obtained. To get a new pressure distribution, pressure equation is formed and calculated. After that, the velocities are reproved and keep forwarding by calculating updated conservative fluxes.

Explicit numerical solution method is solved considering all the variables as known variables at the previous time step. However, implicit numerical solution method would use some or all of the variables as unknown variables for the next time step. This SIMPLE algorithm is called “Semi-Implicit Method”, as it solves momentum equation and pressure correction equation implicitly but the velocity correction equation explicitly. The simulation results are accurate by second order both in time and space.

The domain used for this study has two regions, an inner region, and an outer region where the inner region is constructed with a semi-circle front end with a radius of 2.5c with a center at c/4 location of the airfoil at the upstream and a rectangular region with a width of 2.5c at the downstream. The whole inner region mesh is generated using an unstructured triangular grid. The outer region is constructed with a C-type structured mesh with a radius of 25c and a rectangular design at the wake of the airfoil with a length of 30c (Figure 8).

The semi-circular region of the outer domain is used as the velocity inlet and the other side of the outer region has been used as the pressure outlet.

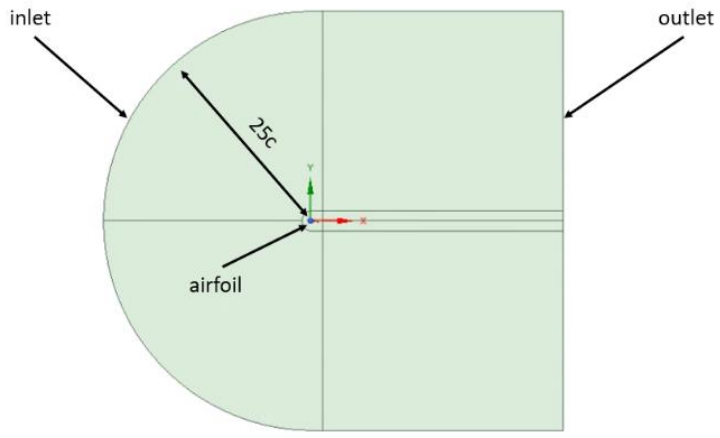

Figure 8: Computational domain.

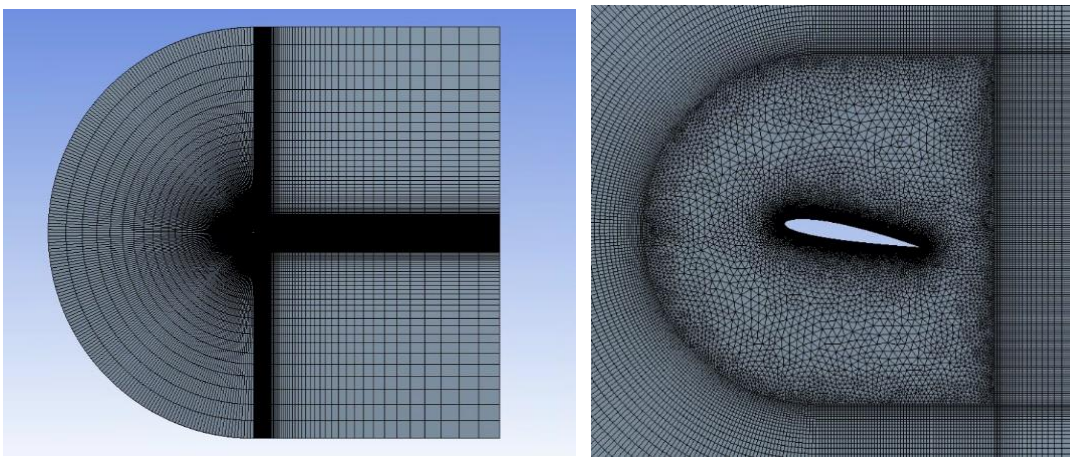

Figure 9: Meshed computational domain.

The external condition of the flow around all the airfoils is obtained for various angles of attack at Re = 1000. For each analysis, the airfoil is rotated in a clockwise direction for the given angles of attack to keep the wake region constant.

For the thickness distribution of airfoils with NACA 4-digit, the following equation of y_t has been used (Abbott & von Doenhoff, 1959):

$$y_t = \pm \frac{t/c}{0.2} \cdot (0.2969 \cdot \sqrt{x} - 0.1260 \cdot x - 0.3516 \cdot x^2 + 0.2843 \cdot x^3 - 0.1015 \cdot x^4) \quad (3)$$

Where the range of x is xϵ [0 1] and the maximum thickness to chord ratio is t/c. This ratio can be found in NACA 4-digit airfoils as the last two digits.

The positive direction of the angle of attack is set to be in the clockwise direction. The angles of attack start from 0° to 10° with an increment of 1° per analysis. The pivot point for angles is located at 0.25c from the leading edge of each airfoil.

2.2 Grid Refinement and Time Refinement Study

To validate the analysis, a detailed study of grid and time refinement has been conducted only on NACA 1412. These studies have been conducted for two angles of attack: 5° and 10°. For grid refinement studies, three different meshes have been applied as coarse, medium, and fine meshes. Node and element numbers of the domain for each mesh are enlisted in Table 2. The time increment used for grid refinement study is $\Delta t = 0.005$ s. The simulations are conducted until t = 100 s which can be converted as a non-dimensional time, $t* = \frac{t*U\infty}{c} = 146$ where the free stream velocity, Uinf = 0.146 m/s, and chord length, c = 0.1 m. The computational time interval is t*ϵ [0 146] for the simulations. In this study, the main concern is to analyze the behavior of the airflow after the results reach a steady-state or periodic condition. Therefore, the initial behavior of the solution is ignored.

Table 2: Meshes of NACA 1412 at α = 5° and 10°

Meshes	**Nodes around the airfoil**	**Total number of Elements**
Coarse	63923	77206
Medium	93319	108638
Fine	130735	146366

Grid refinement study demonstrates that all three meshes result in approximately the same aerodynamic coefficients at the initial start region. The results reach a quasi-steady solution at t*=19.4 and stay the same throughout the whole simulation. Therefore, depending on this outcome, the rest of the simulations have been conducted using medium mesh as the differences are quite negligible as shown in Figure 10.

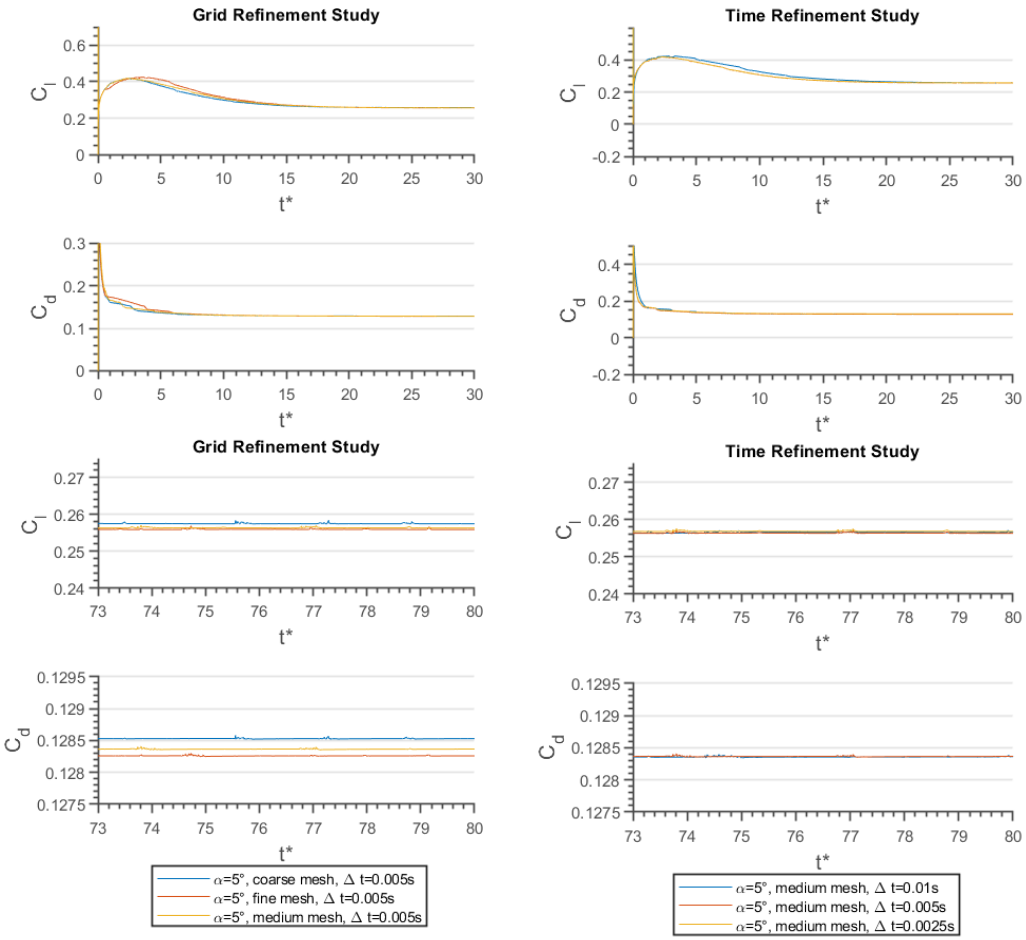

Figure 10: Instantaneous lift and drag coefficients for the grid refinement and time refinement studies in the left and right column respectively during t*ϵ [0 30] (top two rows) and during t*ϵ [73 80] (bottom two rows) for α=5°.

For α=10°, the instantaneous aerodynamic forces are also found to be very close to each other for all three meshes investigated with a phase shift. That phase shift occurred due to the unsteadiness and flow separation at this angle of attack. However, the period of the oscillation and amplitude of the oscillation is very close to each other for all three mesh configurations investigated.

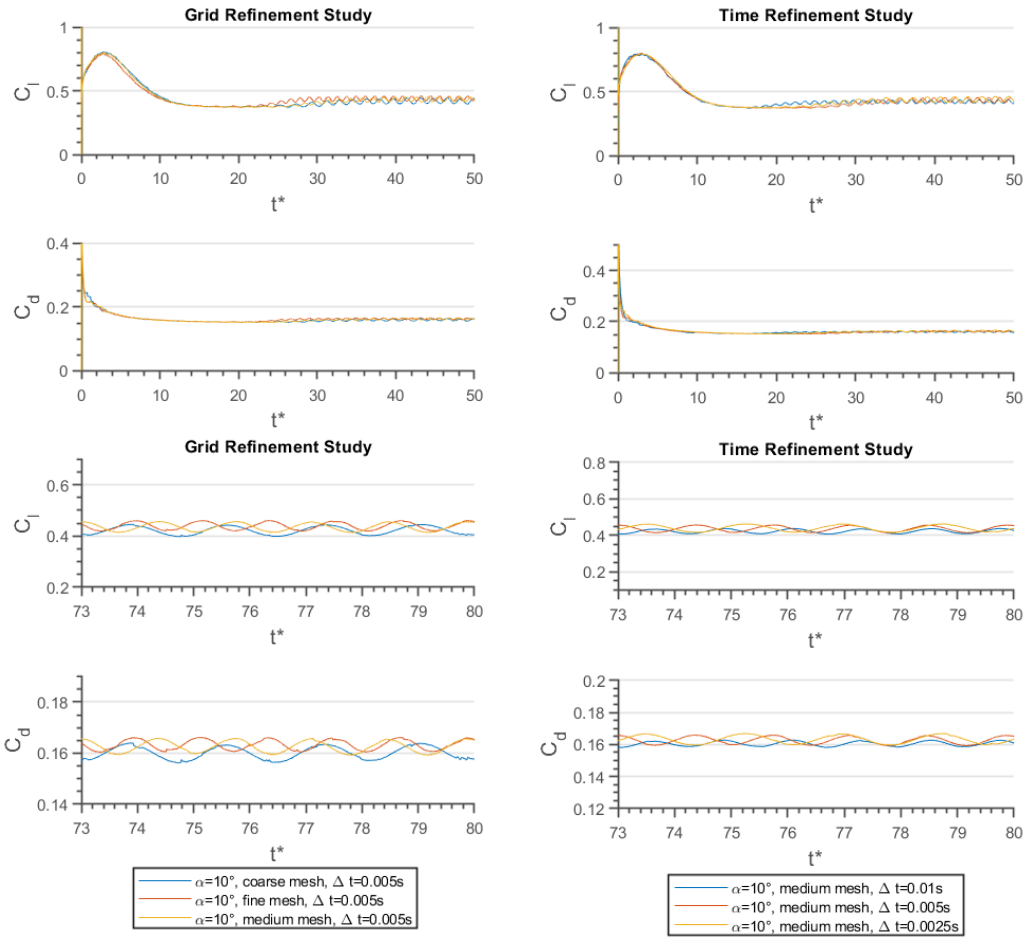

Figure 11: Instantaneous lift and drag coefficients for the grid refinement and time refinement studies in the left and right column respectively during t*ϵ [0 30] (top two rows) and during t*ϵ [73 80] (bottom two rows) for α=10°.

Similarly, a time refinement study has also been conducted for three-time increments (Δt) with 0.01s, 0.005s, and 0.0025s and with the medium mesh.

At α=10°, the results for time step 0.01s phase out at t*=16.1 and follow a cyclic pattern throughout the simulation. Phase shifts are visible between the three-time increments but the frequency and the amplitude of the oscillations are close to each other.

All the results for grid refinement and time refinement studies at α=5° and α=10° for time intervals of t*ϵ [0 30] and t*ϵ [73 80] are represented in Figure 10 and Figure 11, respectively.

2.3 Validation Study

It was a difficult task to find a suitable study from where this present study could be validated as there is not much literature studies both in computational and experimental field on cambered airfoils at very low Reynolds number flight regime.

However, the results of the current study are also compared with the INS2d simulations conducted by Kunz (P. J. Kunz, 2003) for NACA 4402 airfoils at Re=1000 for angles of attack with a range starting from 0° to 10° for fully laminar flow (Figure 12).

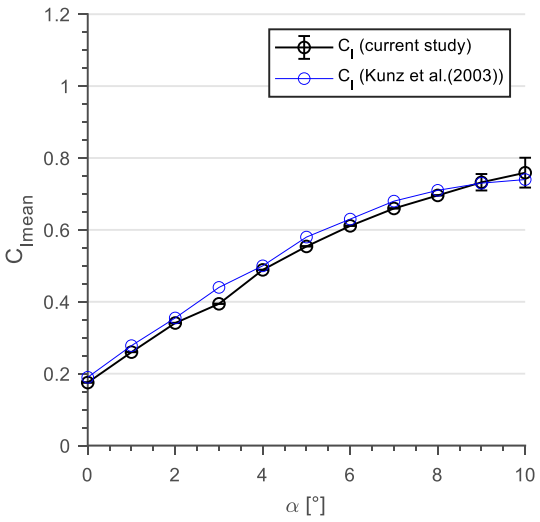

Figure 12: Comparison of mean lift coefficient with the data found from literature for Re=1000.

In Figure 12, a similar lift curve pattern is observed and both analyses indicate a similar reduction in the lift curve slope as well for the mean lift coefficient. In general, the comparison between these two analyses provides validation for the current study for low angles of attack. As the unsteadiness in the flow increases, the

aerodynamic force coefficients are found to differ at higher angles of attack of 9° and 10°. At 10°, the mean lift coefficient shows a negligible slightly higher value than the Kunz results. However, because of the difference of simulation methods and the meshes, this slight difference is expected therefore neglected in this case.

CHAPTER 3

SOLUTIONS FOR CAMBERED AIRFOILS IN 2D

Four cambered NACA airfoils have been solved for low Reynolds number in order to observe the unsteady aerodynamics around those airfoils, and the main results are discussed further. All the solutions are obtained using different angles of attack ranging from 0° to 10° with an increment of 1°. The main objective of the study is to observe the effect of the camber on the aerodynamic performance of the airfoils at a very low Reynolds number.

3.1 Aerodynamic Coefficients

Figure 13 shows the instantaneous aerodynamic coefficients of NACA 1412 for angles of attack 0° to 10° with an increment of 1°. Figure (a) contains the instantaneous lift coefficients against non-dimensional time step t*. At the starting point (t*=0 to 15), an initial rise is observed which is expected as the simulation starts with an initial assumption that is far from the stable value. Then all the solutions start to converge at t*= 32 and gradually converge afterward. Oscillatory behavior is observed for instantaneous Cl values for the angle of attack of 9° and 10°. This results in a vortex mode shape change from continuous vortex shedding to an alternating vortex shedding configuration (Kurtulus, 2015, 2016).

Similarly, Figure 13b shows the instantaneous C_d value for different angles of attack range starting from 0° to 10°. The values start to converge at t*=32 and only oscillations are observed for angles of attack 9° and 10°. The mean lift coefficient ($\overline{C_l}$) and mean drag coefficient ($\overline{C_d}$) for different angles of attack for 0° to 10° at Re=1000 for NACA 1412 is presented in Figure 14 with error bars denoting the minimum and maximum oscillations of the unsteady amplitudes in the interval where the mean values (presented as black circles) are considered.

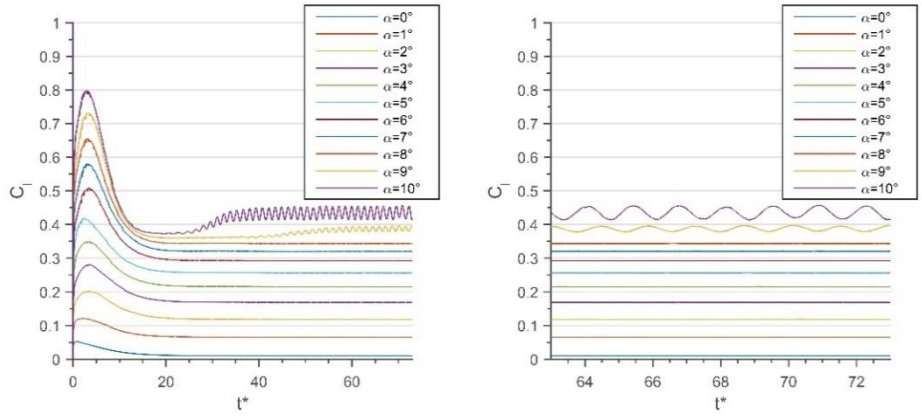

a) Instantaneous lift coefficient

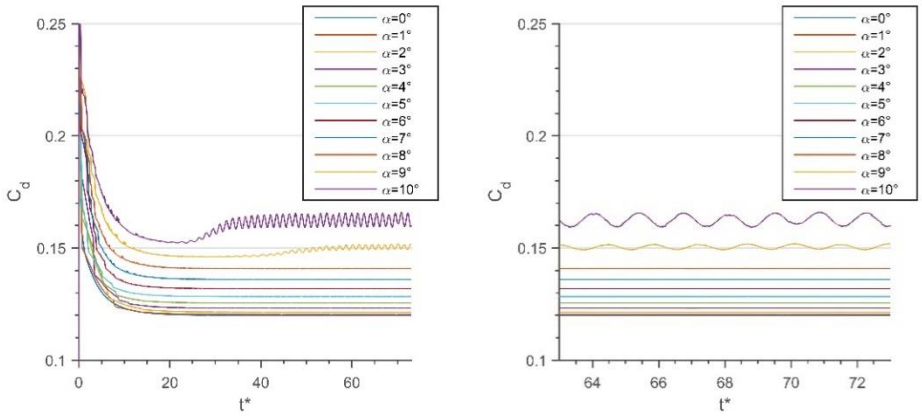

b) Instantaneous drag coefficient

Figure 13: Instantaneous aerodynamic coefficients of NACA 1412 at angles of attack starting from 0° to 10° at Re=1000.

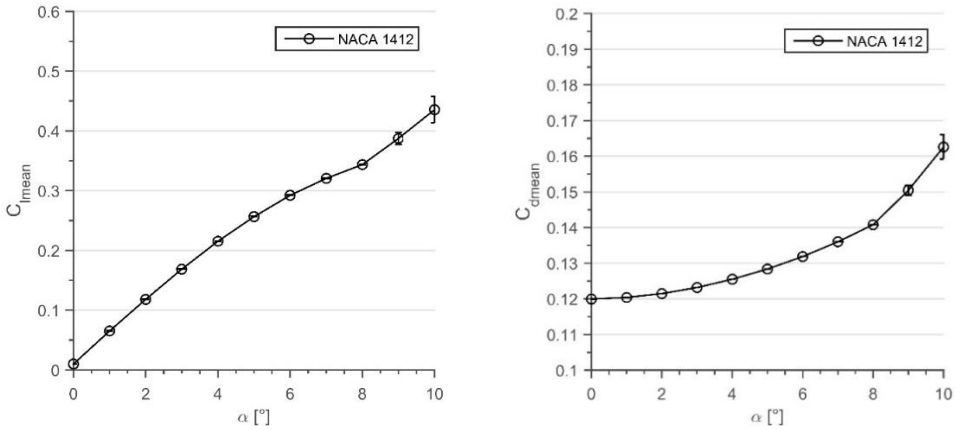

Figure 14: Mean aerodynamic force coefficients of NACA 1412 at different angles of attack.

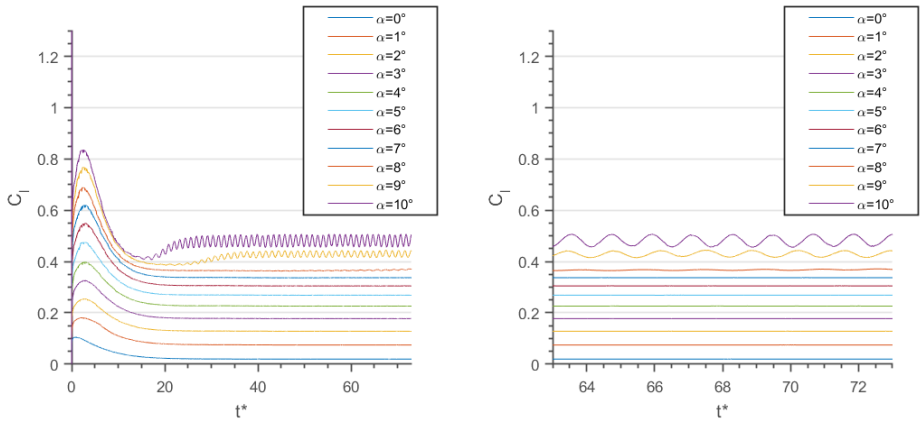

a) Instantaneous lift coefficient

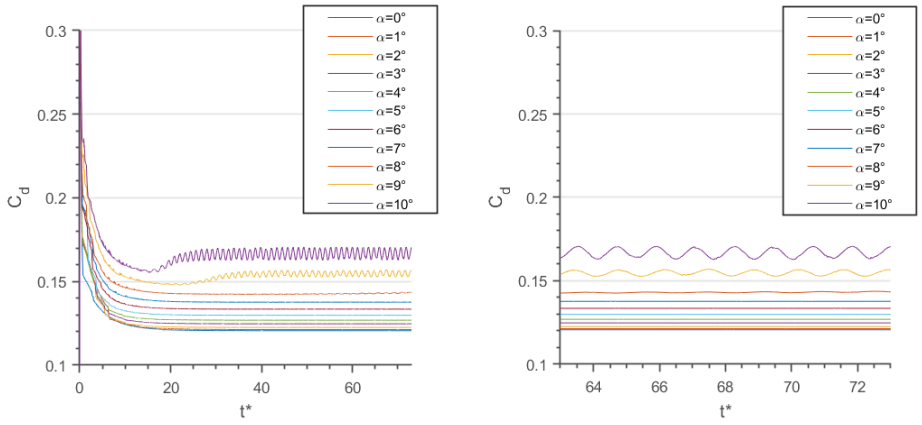

b) Instantaneous drag coefficient

Figure 15: Instantaneous aerodynamic coefficients of NACA 2412 at angles of attack starting from 0° to 10° at Re=1000.

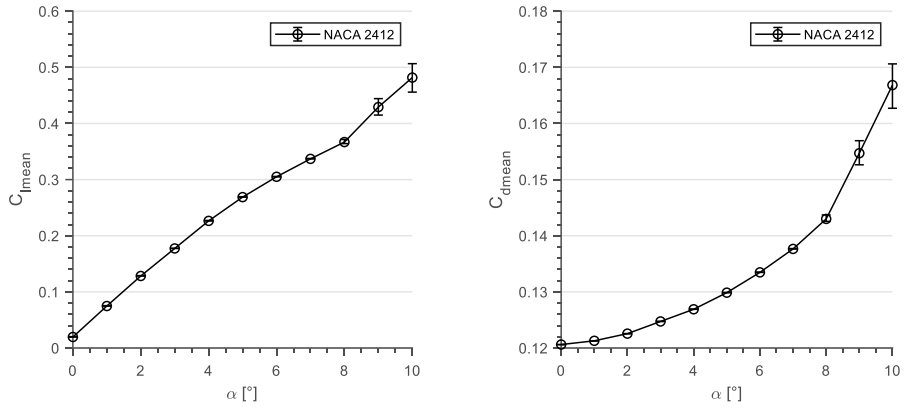

Figure 16: Mean aerodynamic force coefficients of NACA 2412 at different angles of attack.

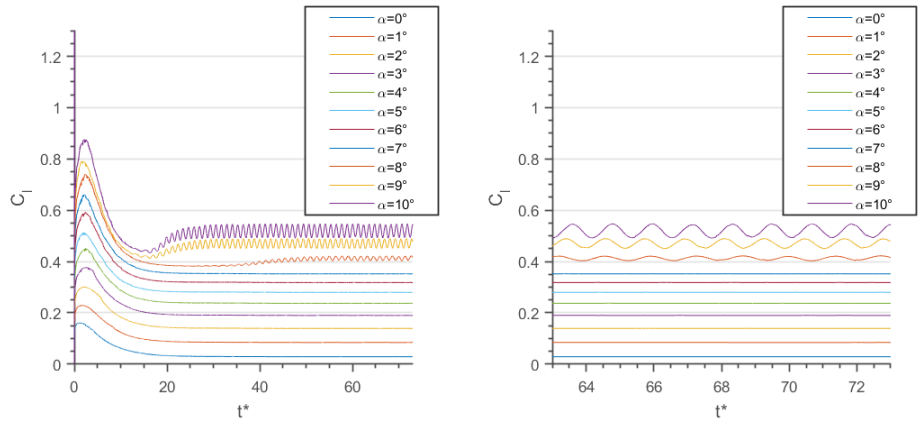

a) Instantaneous lift coefficient

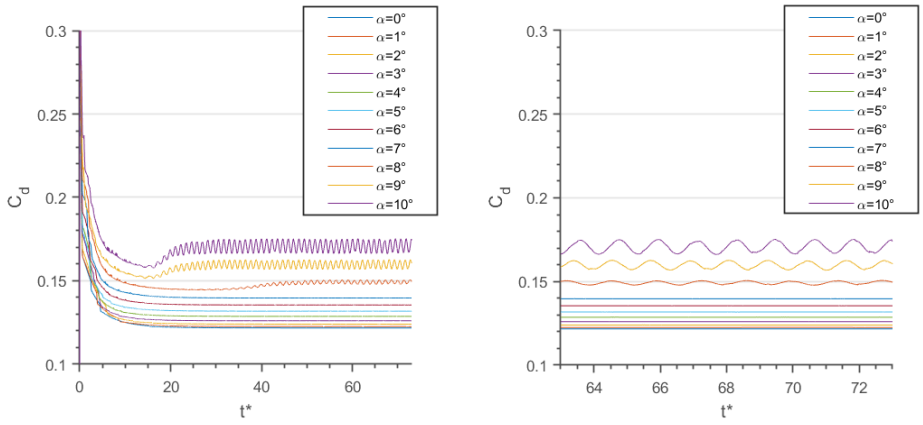

b) Instantaneous drag coefficient

Figure 17: Instantaneous aerodynamic coefficients of NACA 3412 at angles of attack starting from 0° to 10° at Re=1000.

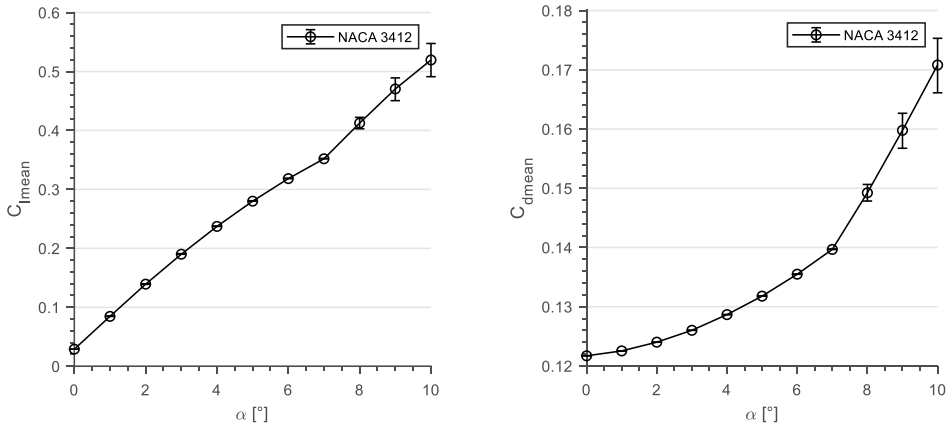

Figure 18: Mean aerodynamic force coefficients of NACA 3412 at different angles of attack.

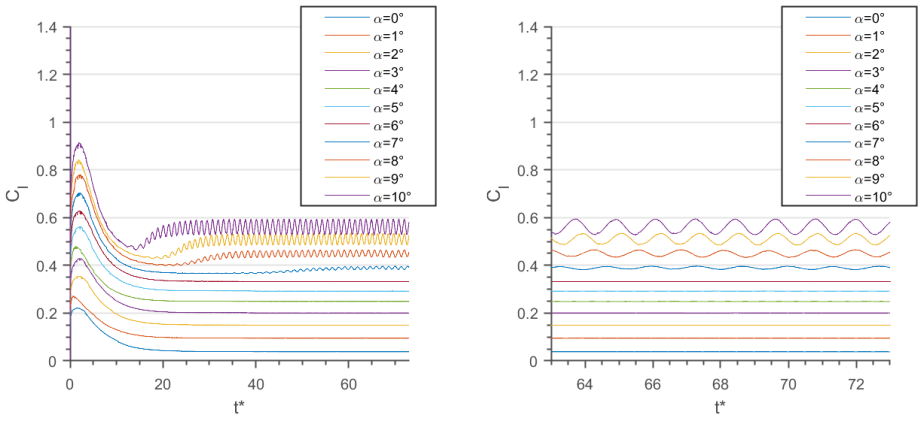

a) Instantaneous lift coefficient

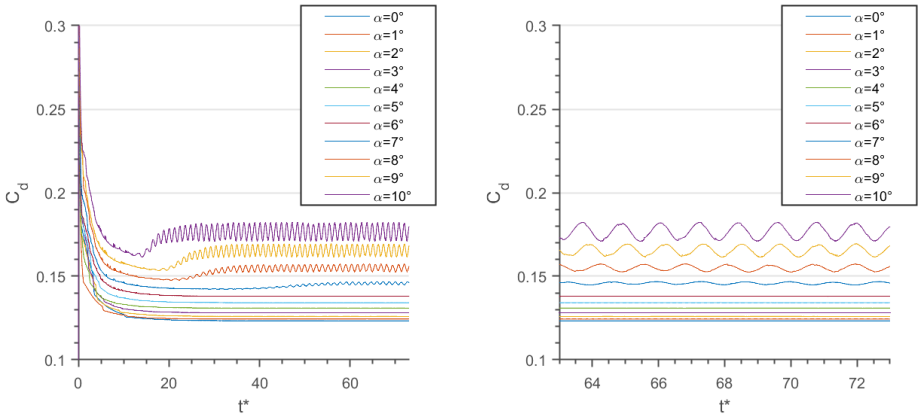

b) Instantaneous drag coefficient

Figure 19: Instantaneous aerodynamic coefficients of NACA 4412 at angles of attack starting from 0° to 10° at Re=1000.

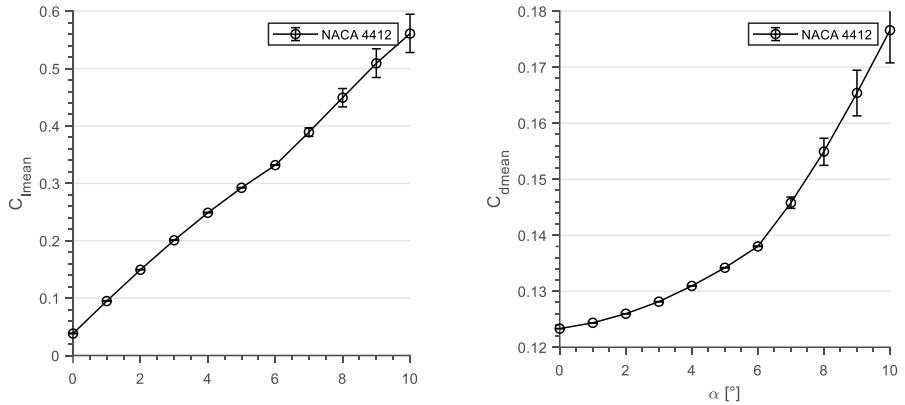

Figure 20: Mean aerodynamic force coefficients of NACA 4412 at different angles of attack.

For calculating the mean Cl and Cd values, firstly, the arithmetic average (mean) of the results is calculated and then maximum and minimum values are calculated to show the deviation from the mean value. A gradual increase in lift curve is noticed as the angle of attack increases from 0° to 10° which is different than the high Reynolds number lift coefficient curves having a linear trend until the stall angle.

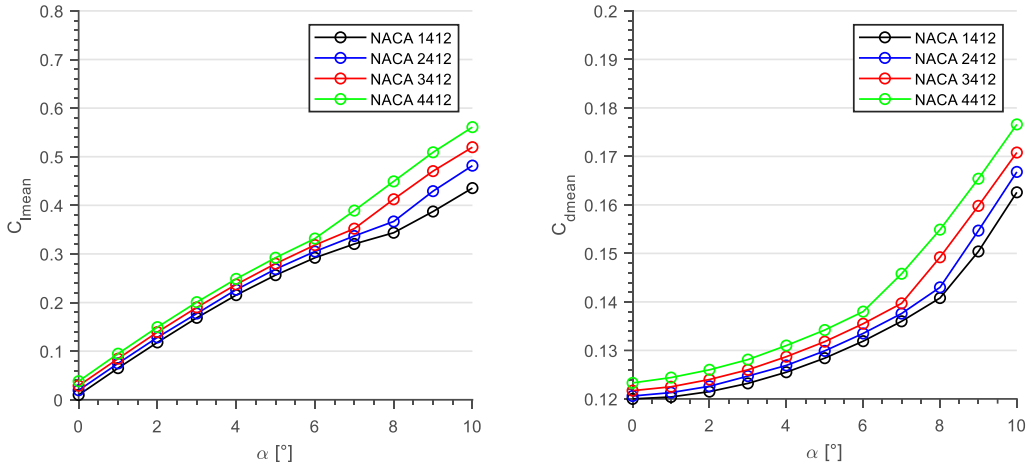

Figure 21: Comparison of mean aerodynamic coefficients for different airfoils.

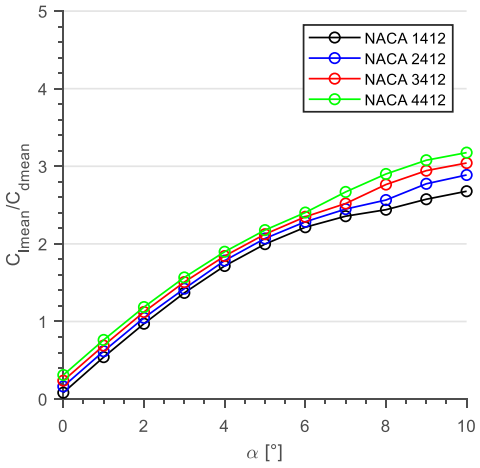

Figure 22: Comparison of mean C_l/C_d value for different airfoils.

A clear view of how $\overline{C_l}/\overline{C_d}$ value changes according to angle of attack is presented in Figure 22.

Figure 15 to Figure 20 show the results obtained for NACA 2412, NACA 3412, and NACA 4412 including both instantaneous and mean lift coefficient and drag coefficient for different angles of attack ranging from 0° to 10° for Re=1000.
Figure 21 and Figure 22 show comparisons of aerodynamic coefficients between the four cambered NACA airfoil profiles; NACA 1412, NACA 2412, NACA 3412, and NACA 4412 at Re=1000 for different angles of attack.

3.1.1 Influence of angle of attack

Figure 20-22 show the relative comparison of four cambered NACA airfoils according to the increasing angle of attack. As the angle of attack increases, the discrepancy between the mean aerodynamic coefficients increases. The increment is significant at the higher angle of attack; especially starting from $\alpha = 8°$ to $\alpha = 10°$. Although a higher angle of attack creates flow separation on airfoils, it becomes insignificant as a higher lift-to-drag ratio compensates for the results.

3.1.2 Influence of camber

The effect of relative camber is presented in Figure 21 for four cambered NACA airfoils of relative camber 0.01, 0.02, 0.03, and 0.04. As the maximum camber of the airfoils increases, the mean lift coefficient increases but so as the drag coefficients. For example, at the angle of attack of 10°, each 1% increase in camber leads to around 7-9% increase in mean lift coefficient and around 2.5% in the mean drag coefficient. Figure 22 clearly shows the significant increase in Cl/Cd with the relative camber. At $\alpha=10°$, NACA 1412, NACA 2412, NACA 3412, and NACA 4412 have mean Cl/Cd values of 2.6784, 2.8879, 3.0422, and 3.1231 respectively, showing an around 5-7% of change per 1% maximum camber increase. It's a considerable trade-off in terms of MAVs wing design.

3.2 Pressure Distributions

A relative comparison of instantaneous pressure distributions around the cambered NACA airfoils are presented in Figure 23 and 24 for α=9° and 10° as these two angles of attack show unsteady behavior.

For α = 9° and 10°, the velocity streamlines are also demonstrated below each pressure distribution figure so that one can relate the pressure distribution on airfoils.

Vortex patterns are highly dependent on the angle of attack and moderately to the camber distribution. In order to understand the patterns, instantaneous streamlines are compared for each airfoil at α=0°, 5°, 7°, and 8° for Re=1000 in Figure 23.

The trailing edge vortex is found to grow quickly at higher cambered airfoils. The trailing edge vortex is highly visible for NACA 4412 at α=0° compared to NACA 1412, NACA 2412, and NACA 3412 airfoils as shown in Figure 23.

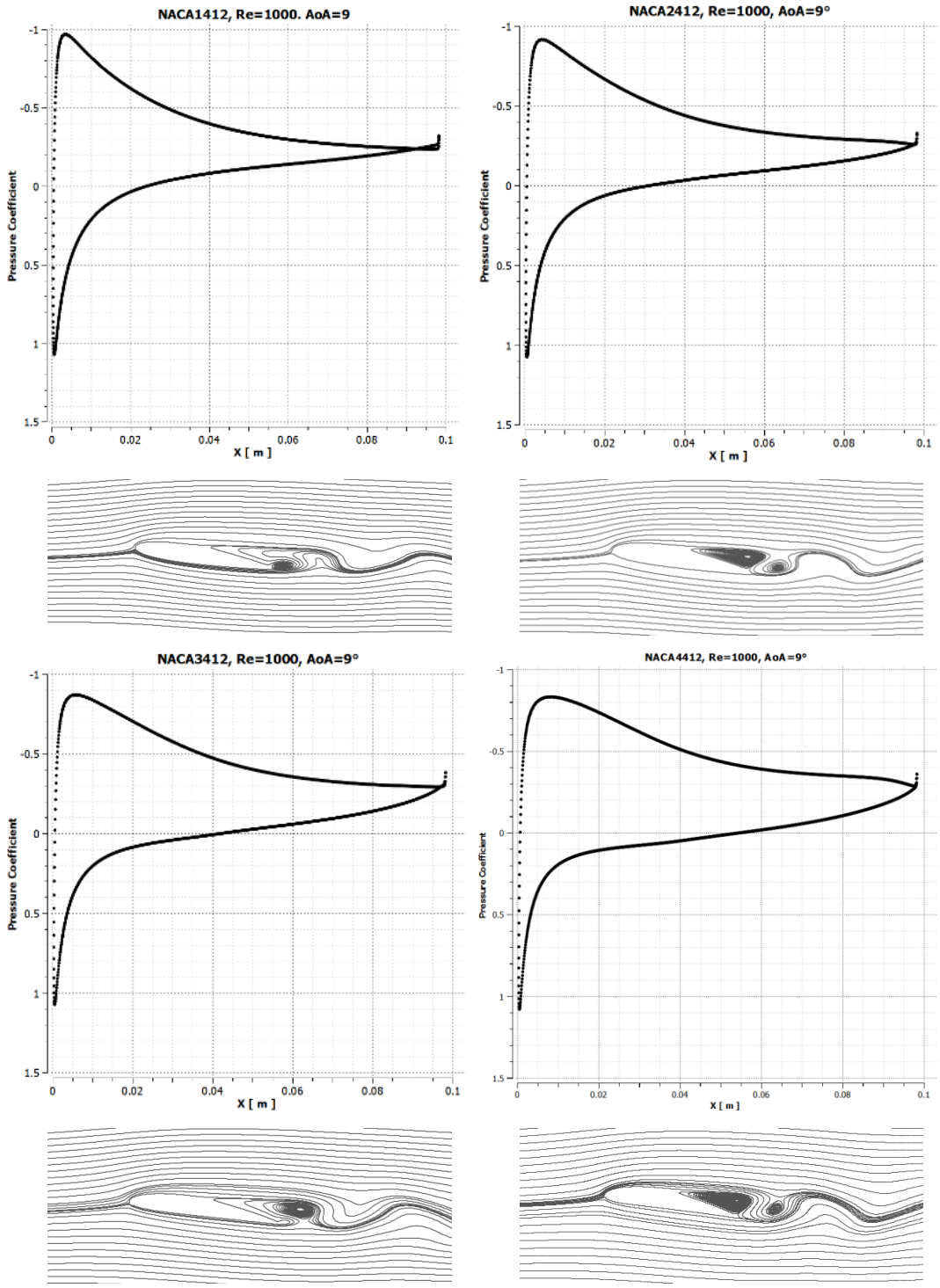

Figure 23: Instantaneous pressure distributions and streamlines around NACA1412, NACA2412, NACA3412, and NACA4412 at α = 9° at t*=73.

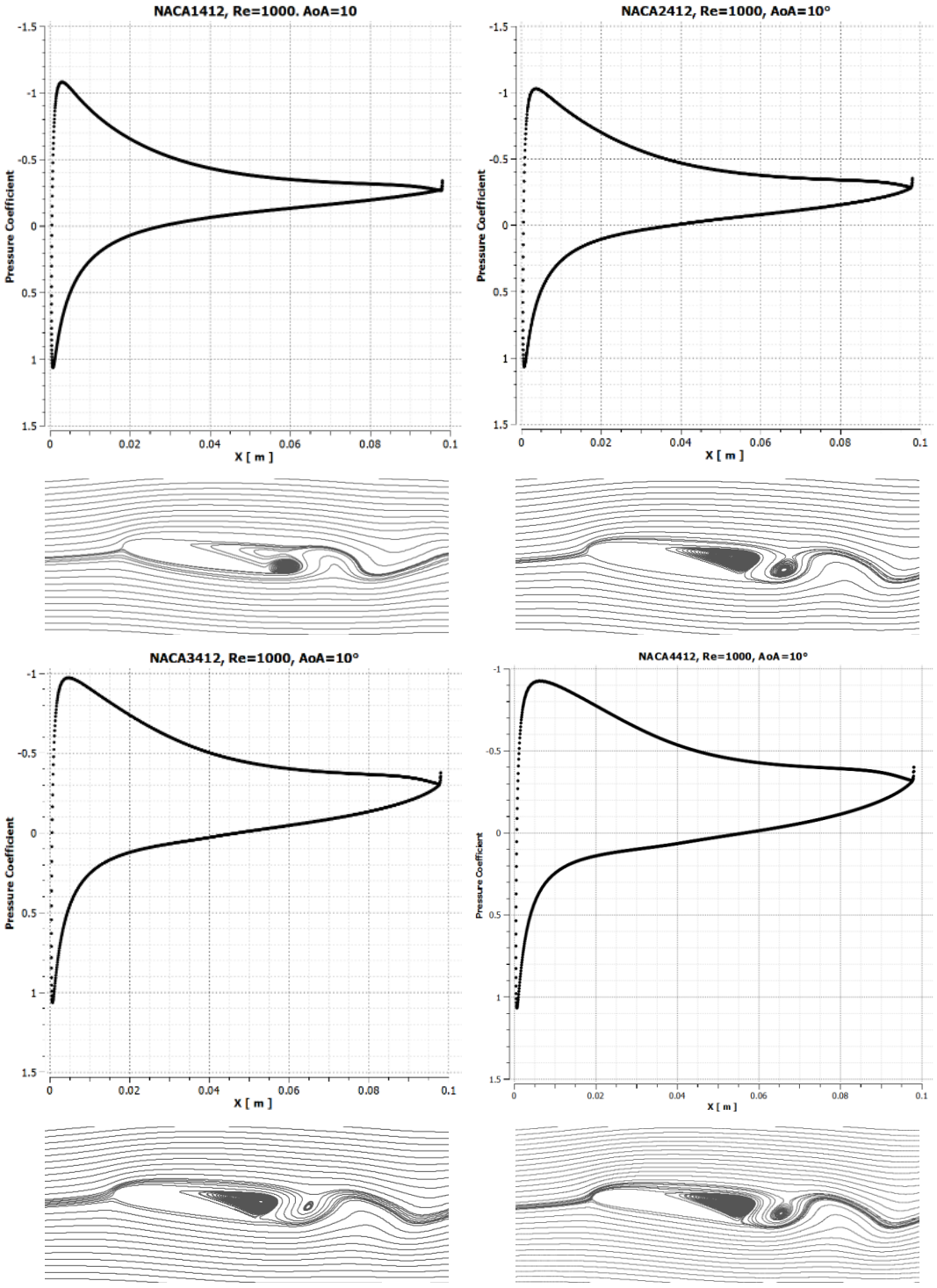

Figure 24: Instantaneous pressure distributions and streamlines around NACA1412, NACA2412, NACA3412, and NACA4412 at α = 10° at t*=73.

NACA 1412 **NACA 2412**

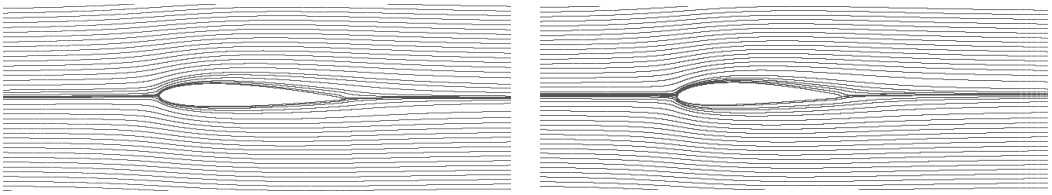

α = 0°

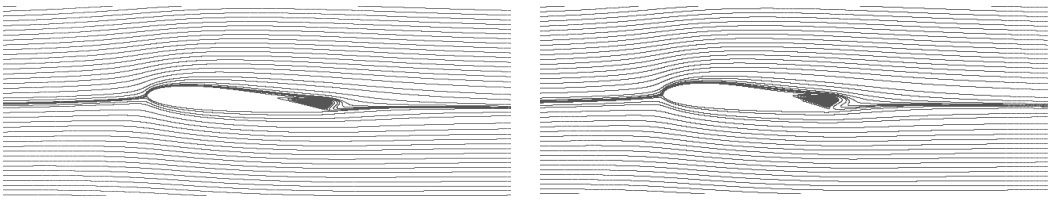

α = 5°

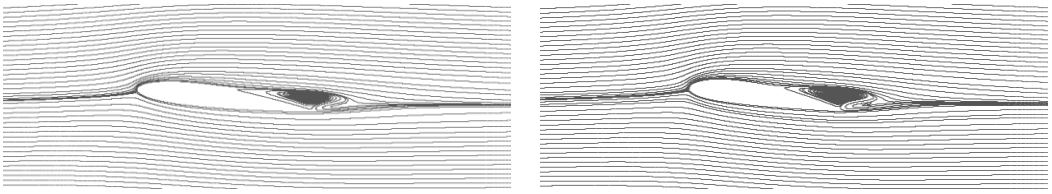

α = 7°

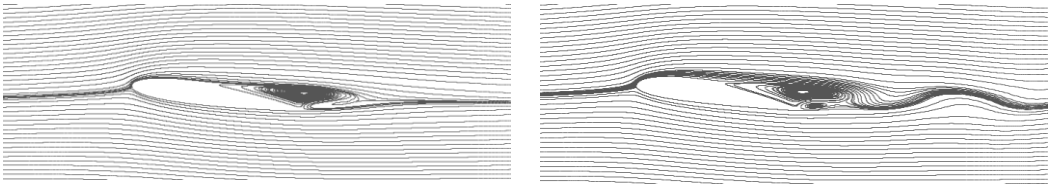

α = 8°

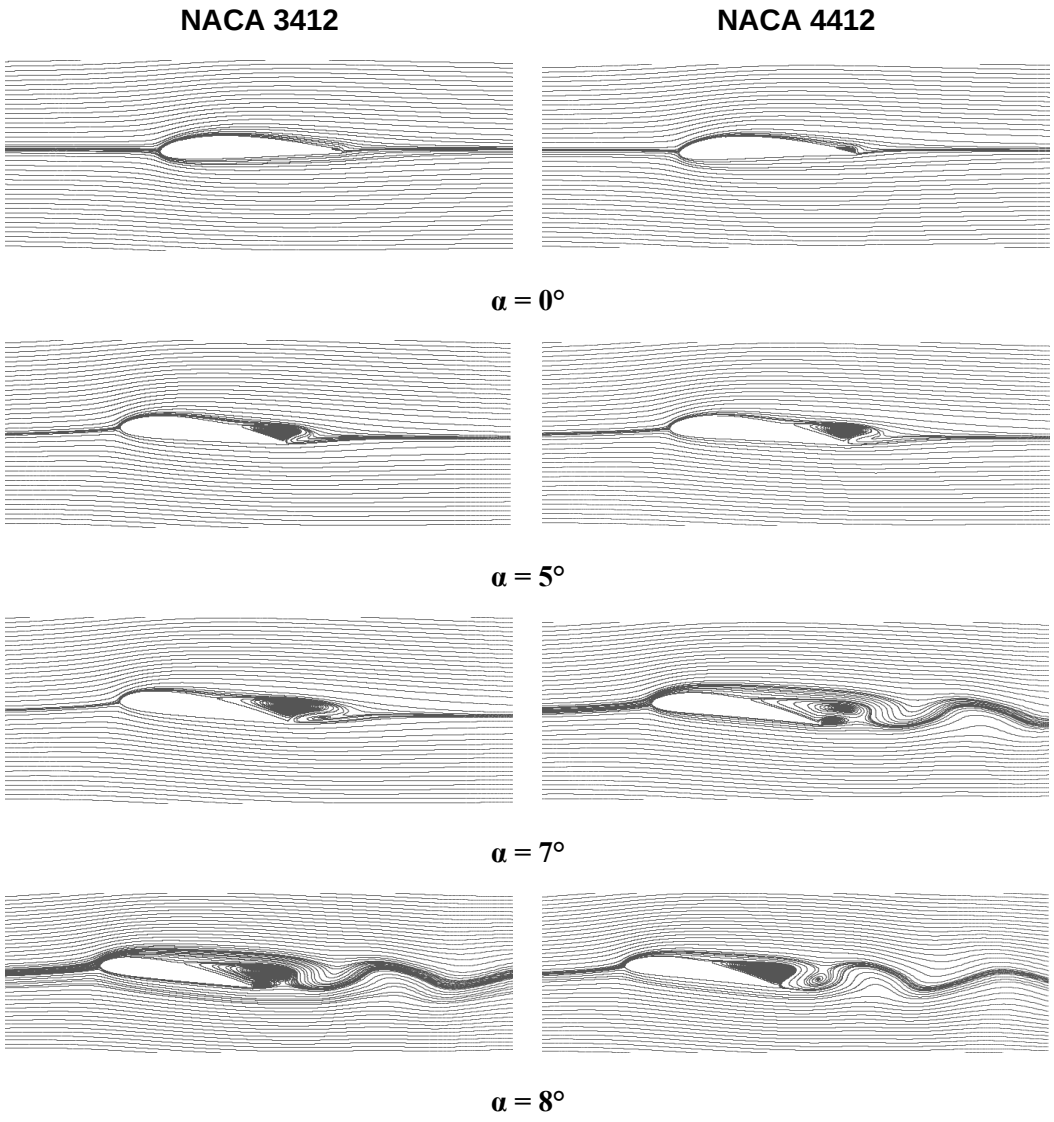

Figure 25: Streamline patterns of instantanous velocity for angles of attack 0°, 5°, 7° and 8° for NACA1412, NACA2412, NACA3412, and NACA4412 for Re=1000.

3.2.1 Influence of angle of attack

Pressure distributions around the cambered NACA airfoils are obtained and presented in Figures 23-24. For a higher angle of attack the pressure distribution around the airfoil increases on the upper surface as well as the lower surface. As the angle of attack increases, the separation point moves towards the leading edge of the

airfoil causing an increase in the magnitude of suction pressures on the upper surface both in the leading edge and trailing edge.

3.2.2 Influence of camber

The relative difference of pressure distribution according to the camber is observed in Figures 23-24. The airfoils with higher camber have a gradual decrease in negative pressure on the upper surface compared to the airfoils with lower camber. This indicates that the airfoils with higher cambers have a longer flow separation region resulting in a higher lift at the same angle of attack than the airfoils with lower camber.

3.3 Skin Friction Coefficient

At very low Reynolds numbers, due to viscous effects in the flow, the boundary layer becomes very thick on the airfoil and flow separation may occur even at smaller angles of attack. Therefore, the study of flow separation is very important in this kind of analysis where the Reynolds number is very low.

Flow separation positions can be determined by observing the skin friction coefficient values. In the position of flow separation, the skin friction coefficient will be zero as there will be no attachment to the flow with the airfoil surface.

Flow separation positions may vary due to maximum camber, angle of attack, or Reynolds number. A brief comparison between different airfoils with different maximum camber distributions at angles of attack of 9° and 10° are represented in Figures 26 and 27. The separation points are marked with red dots on airfoil profiles where the skin friction coefficient is equal to zero.

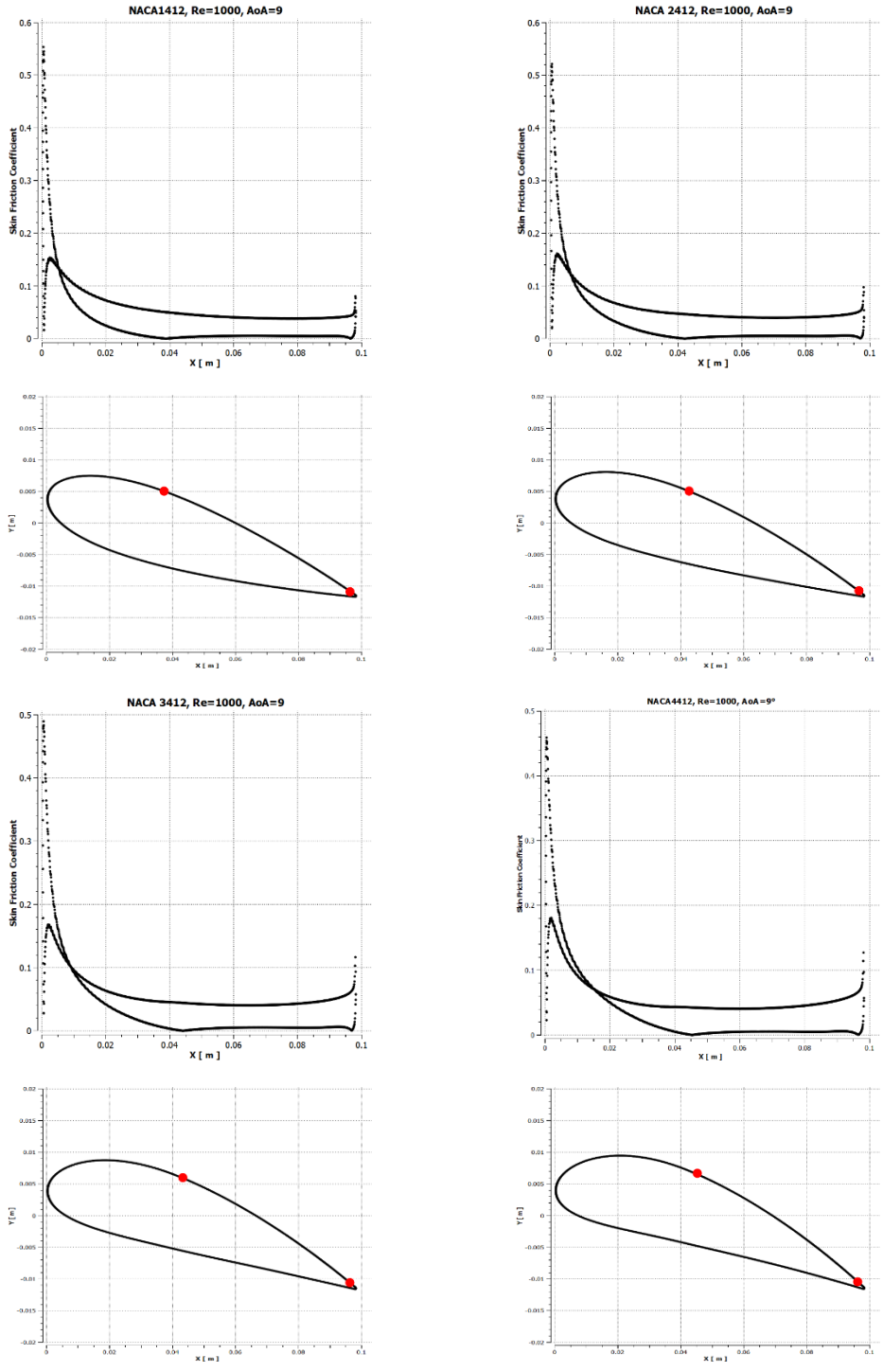

Figure 26: Skin friction coefficient distribution and marked out separation points on NACA 1412, NACA 2412, NACA 3412, and NACA 4412 at α = 9°.

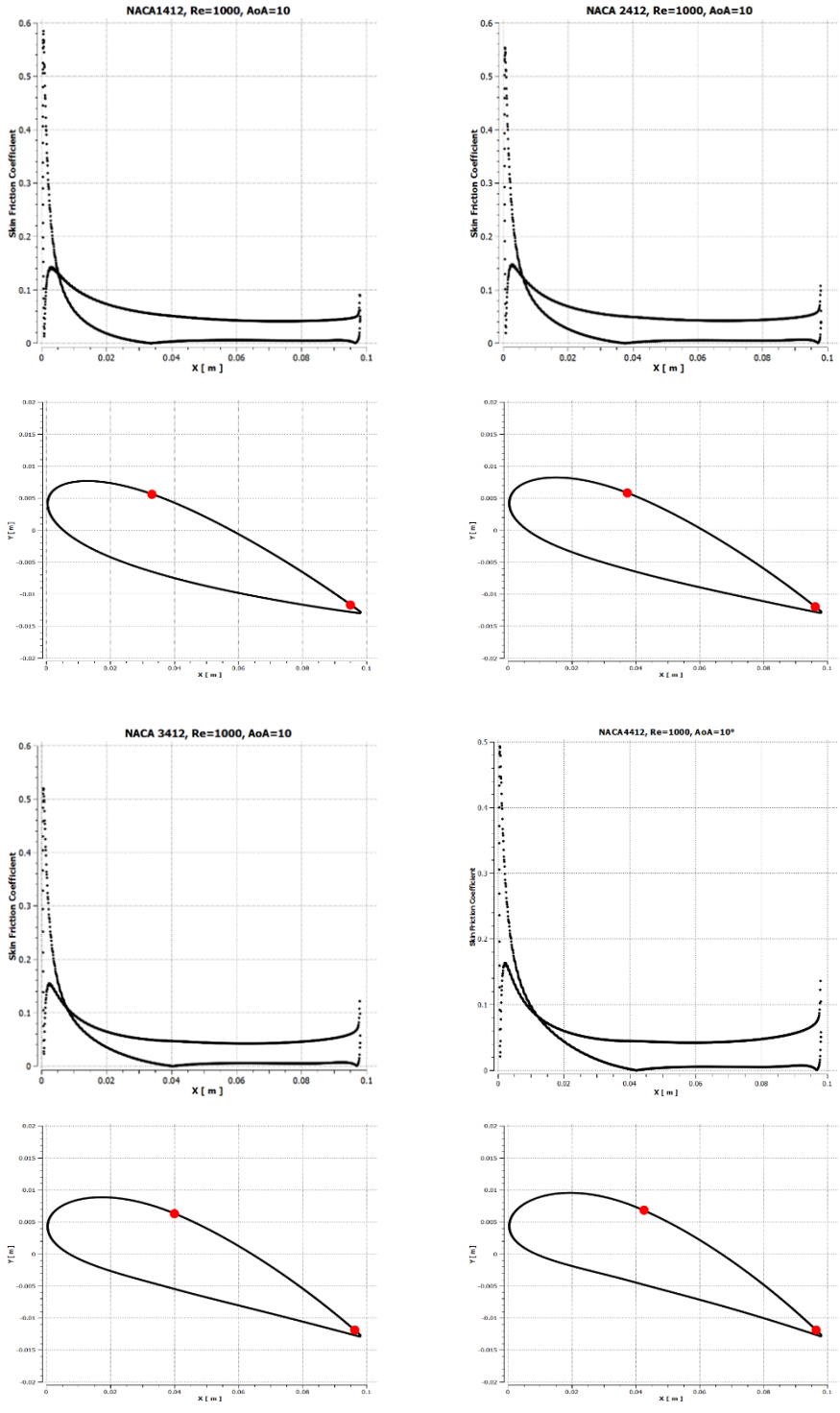

Figure 27: Skin friction coefficient and separation point on NACA 1412, NACA 2412, NACA 3412, and NACA 4412 at $\alpha = 10°$.

3.3.1 Influence of angle of attack

Skin friction coefficients and the relative airfoils are demonstrated in Figure 26 and Figure 27. Only angles of attack 9° and 10° are showed in here for four different cambered NACA airfoils in order to understand the flow separation behavior.

The angle of attack plays the main role in the flow separation positions. As the angle of attack increases the flow separation point shifts towards the leading edge and the separation length increases as well. However, the flow separation does not occur until the angles of attack 4°. At higher angles of attack the flow separations are more visible and thus pointed out in Figures 26 and 27.

3.3.2 Influence of camber

Relative camber magnitude has a huge influence on the flow separation as shown in Figures 26 and 27. Four different airfoils with four different maximum camber; 1%, 2%, 3%, and 4% are compared in those figures.

It can be noticed that as the maximum camber increases, the initial flow separation points shift towards the rear side. In addition, airfoil with a 4% maximum camber has a longer flow separation region than the ones with 3%, 2%, or 1%.

Therefore, increasing the maximum camber can be a way of delaying flow separation position towards the trailing edge when designing MAV wings.

3.4 Strouhal Number Analysis

Strouhal number, a dimensionless parameter is another indicator of whether the flow is generating a vortex or not. The flapping frequencies and amplitudes of 42 species of birds, bats, and insects are analyzed in cruise flight by Taylor et al (Taylor et al., 2003) and found out that the average range of Strouhal number between 0.2 and 0.4 at which these flying animals fly. This study gives a basic idea of what to be expected from future flapping airfoil simulations in a low Reynolds number regime.

Strouhal number can be defined as,

$$St = fA/U \tag{4}$$

where f is the flapping frequency in Hertz, A is the characteristic length, and U is the flight speed. A is taken as the diameter when the flow is over a cylinder, but for flow over flapping airfoil it is normally taken as the chord length of the wing.

Analysis of Taylor et al demonstrated that the Strouhal number can be used as a parameter for comparing flight performances of different flying animals no matter what the size is as the Strouhal number is dimensionless. High Strouhal number indicates that the flow is dominated by viscosity where the oscillating movement of the flow can be observed. On the other hand, a low Strouhal number means the fast-moving fluid suppresses the vortices and does not allow them to be formed.

To observe the four NACA airfoil profiles, amplitude spectrums have been obtained using Fast Fourier Transform (FFT) algorithm based on the lift coefficients. Then Strouhal numbers have been calculated using those amplitude spectrums of lift coefficients. To avoid the initial errors of the computations, the data between 51.1<t*<73 have been used for the calculations. Maximum frequencies of the lift coefficient amplitude spectrums are labeled. To understand the effect of angle of attack on cambered airfoils, four NACA airfoil profiles: NACA 1412, NACA 2412, NACA 3412, and NACA 4412 are analyzed for α = 0°, 5°, 7°, and 10°. Figure 28 demonstrates the Strouhal number related to each airfoil for mentioned angles of attack. For all these four airfoil simulations, the amplitude is highest for α = 10°

however the oscillation may start for the low angle of attack as well. As the angles of attack increase, so as the Strouhal number until a local amplitude peak is generated for the high cambered airfoil.

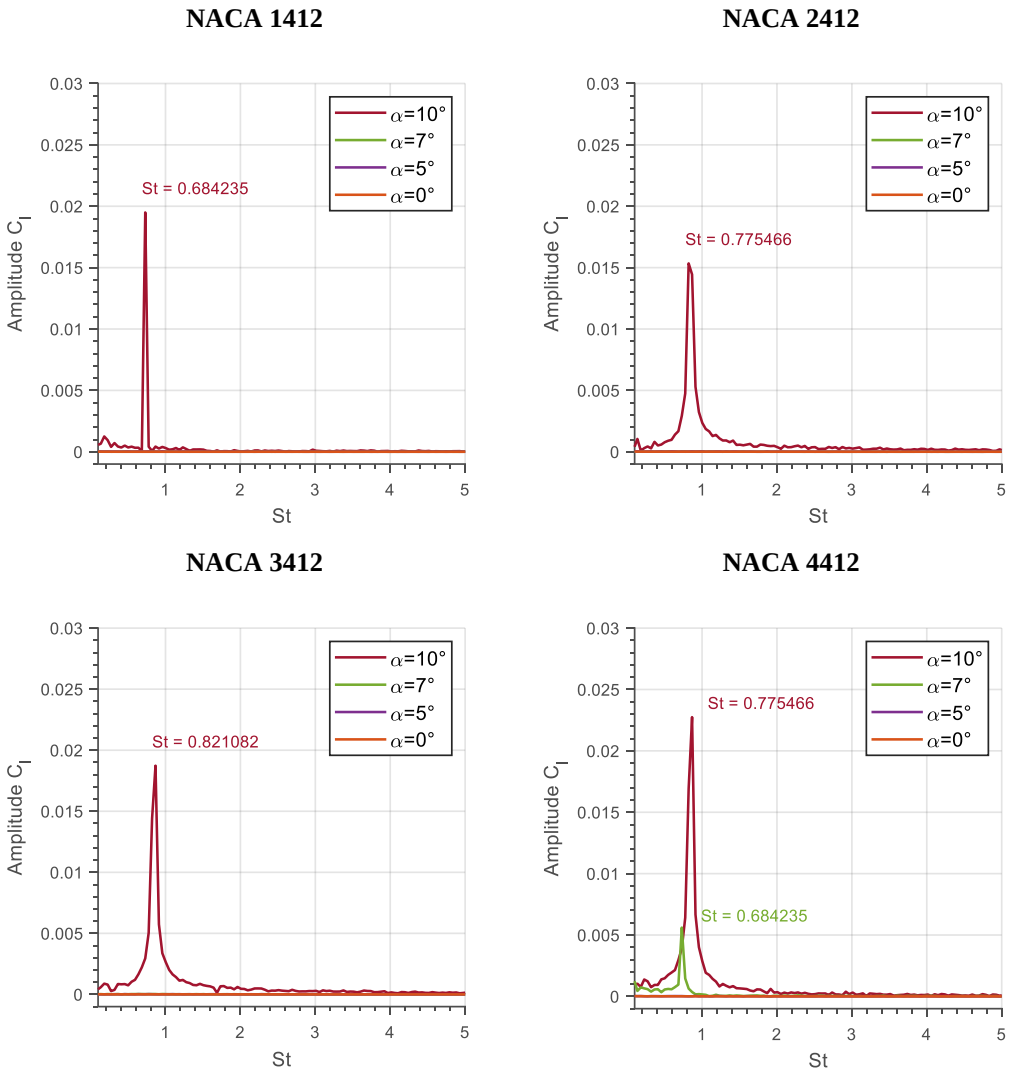

Figure 28: Amplitude spectrum of NACA 1412, NACA 2412, NACA 3412, and NACA 4412 at α = 0°, 5°, 7°, and 10° for 51.1<t*<73.

The maximum Strouhal number is observed at α = 10° for NACA 3412 with St = 0.82. For NACA 1412, NACA 2412, and NACA 3412, no sort of characteristic frequency is detected at α = 7° or below. However, for NACA 4412, a peak value is

observed for α = 7° with St = 0.68 meaning the vortex shedding starts at α = 7° for NACA 4412.

To have a clear understanding of the camber effect on vortex formation, lift coefficient distribution, and Strouhal number of NACA 1412, NACA 2412, NACA 3412, and NACA 4412 have been plotted for α = 7°, 8°, 9°, and 10° in Figure 29. At α = 7°, only NACA 4412 generates an amplitude spike of St = 0.68, and the same outcome can be seen from the lift coefficient distribution in the left column where only NACA 4412 produces oscillation in the wake of the airfoil. However, at α = 8°, the results are a little different as NACA 3412 airfoil starts generating oscillations in the wake flow with a Strouhal number of 0.68 (from the right column) along with NACA 4412 which has a Strouhal number of 0.73. The same scenario can be seen fromthe lift distribution plot (left column) as well, where NACA 4412 and NACA 3412 airfoils generate oscillations in the wake flow. The oscillation wave of NACA 4412 has the maximum amplitude and frequency among other airfoils. NACA 2412 airfoil shows a very slight oscillation at α = 8° and that can be seen from the Strouhal number plot where the green line represents NACA 2412. For a 1° higher angle of attack at α = 9°, the results change a lot. All four airfoils generate vortices meaning they show oscillations in the wake flows. NACA 1412 starts generating vortices at this angle of attack with a Strouhal number of 0.64. At this point, the maximum Strouhal number is seen to be the same for both NACA 4412 and NACA 3412, but NACA 4412 airfoil has the larger amplitude of 0.023, where NACA 3412 has 0.016. The amplitudes and frequencies increase for all four airfoils at α = 10°, where NACA 4412 has the maximum values. NACA 3412 airfoil has the maximum Strouhal number (St = 0.82), and NACA 4412 airfoil has a value of St = 0.78. However, NACA 4412 has a maximum amplitude of 0.023, higher than NACA 3412 airfoil (0.018).

α = 7°

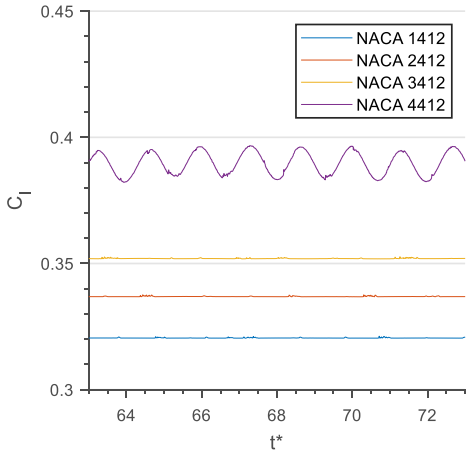
NACA 1412
NACA 2412
NACA 3412
NACA 4412
C_l
t*

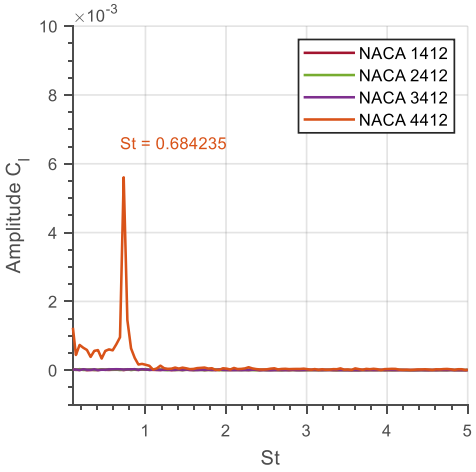
×10^-3
NACA 1412
NACA 2412
NACA 3412
NACA 4412
St = 0.684235
Amplitude C_l
St

α = 8°

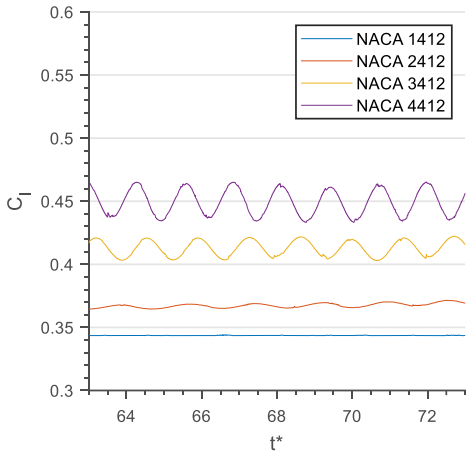
NACA 1412
NACA 2412
NACA 3412
NACA 4412
C_l
t*

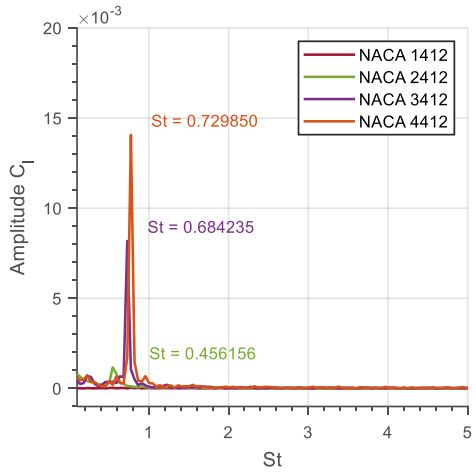
×10^-3
NACA 1412
NACA 2412
NACA 3412
NACA 4412
St = 0.729850
St = 0.684235
St = 0.456156
Amplitude C_l
St

α = 9°

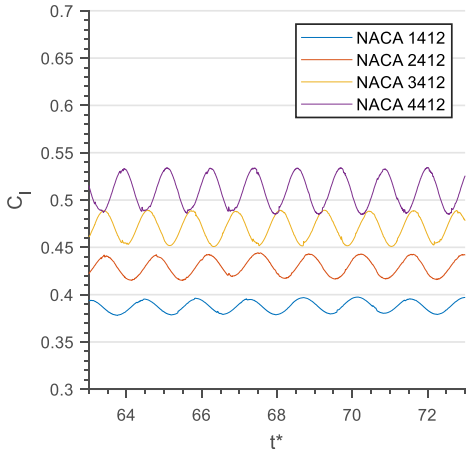
NACA 1412
NACA 2412
NACA 3412
NACA 4412
C_l
t*

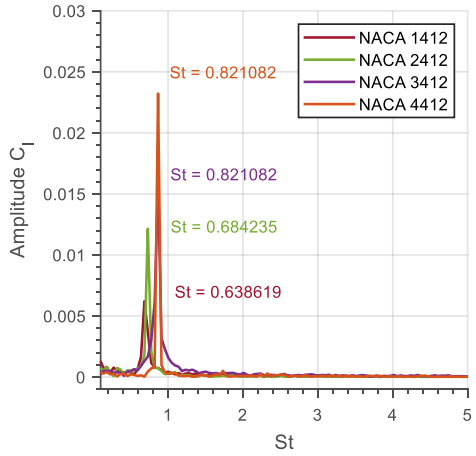
NACA 1412
NACA 2412
NACA 3412
NACA 4412
St = 0.821082
St = 0.821082
St = 0.684235
St = 0.638619
Amplitude C_l
St

α = 10°

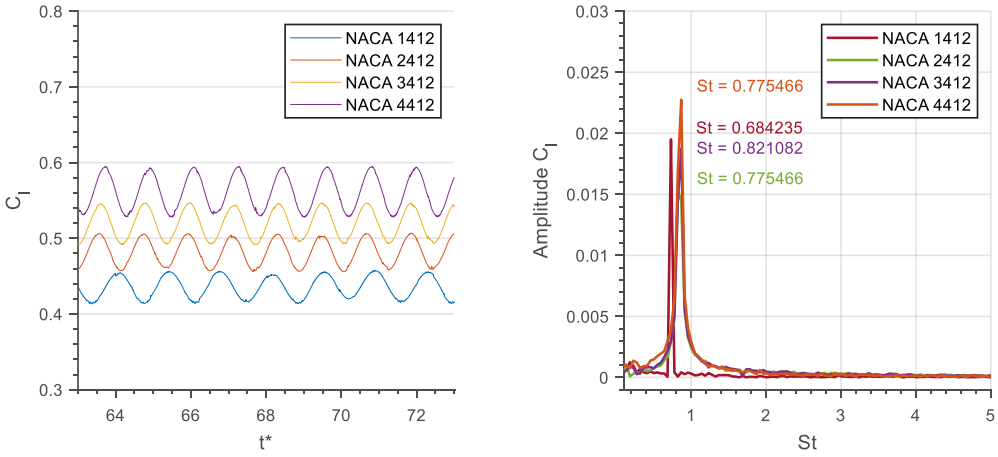

Figure 29: Correlation between lift-coefficient distribution (left column) and Strouhal number (right column) of NACA 1412, NACA 2412, NACA 3412, and NACA 4412 at α = 7°, 8°, 9°, and 10° at Re = 1000.

3.5 Vortex Shedding Patterns of the Airfoils

Most of the studies on vortex shedding patterns at low Reynolds numbers have been conducted on bluff bodies especially on cylinders (Bearman PW, 1966; Roshko A., 1954; Zdravkovich MM, 1996). An alternating vortex shedding can be observed for bluff bodies at certain Reynolds numbers with opposite vortex directions are called Von Karman vortex. Bluff bodies generate drag which introduces lower mean velocity at the wake of the body creating vortices.

There are three basic vortex regions that form behind bluff bodies according to Schaefer and Eskinazi **(Schaefer & Eskinazi, 1959)**: (a) formation region: where the vortex is evolved, (b) stable region: where vortex shows a periodic laminar pattern, and (c) unstable region: where vortex fades away and turbulence starts to build-up for Reynolds number 50 to 125.

An interesting experiment by Strykowski and Sreenivasan involved a small cylinder placed at the wake of a vortex shedding cylinder to control the wake vortex at a low Reynold number **(Strykowski & Sreenivasan, 1990)**. They called the small

cylinder a control cylinder, which had a size of 1/7 of the shedding cylinder, and the whole experiment was conducted at Re = 80. A hydrogen-bubble visualization technique along with numerical simulations demonstrated restricting vortex formation at the wakefield. However, increasing Reynolds number allowed the formation of a vortex pattern. The know-how of vortex shedding formation and its patterns behind airfoils at low Reynolds numbers is important in terms of designing micro air vehicles (MAVs) for better performance and control.

Wake formations and patterns studies in unsteady conditions on airfoils at low Reynolds numbers are usually conducted on pitching or flapping airfoils. A detailed numerical comparison study of unsteady flow pattern in between NACA 0002 and NACA 0012 was conducted by Kurtulus (Kurtulus, 2016), where those airfoils were investigated for a range of angles of the attack starting from 0° to 180° at Re = 1000 for investigating wake vortex formation, vortex shedding frequency, and their end-results on aerodynamics. The main idea of that study was to find the wake flow behavior on symmetric airfoils.

This chapter aims to provide a study on the unsteady flow structure around cambered airfoils at Re = 1000 for a range of angles of attack starting from 0° to 10°. Four 4-digit NACA cambered airfoils have been used: NACA 1412, NACA 2412, NACA 3412, and NACA 4412 for this study.

For each angle of attack, the vortex patterns at the downstream are analyzed for all those four airfoils in order to check the differences. From previous analyses, it can be observed that the oscillation starts from $\alpha = 6°$ for NACA 4412. Therefore, to observe the gradual change in wakefield structure, $\alpha = 5°$, 6°, and 7° are analyzed firstly. Also, Strouhal number distribution for all four airfoils is presented along with each wakefield figure at each angle of attack to visualize the relationship with Strouhal number. At $\alpha = 5°$, all four NACA airfoils do not present any kind of oscillation (Figure 30). They face flow separation but do not produce enough drag to generate oscillation at the wakefield. From the Strouhal number distribution at the right column, it can be observed that there is no spike in Strouhal number for any airfoil at $\alpha = 5°$ as well.

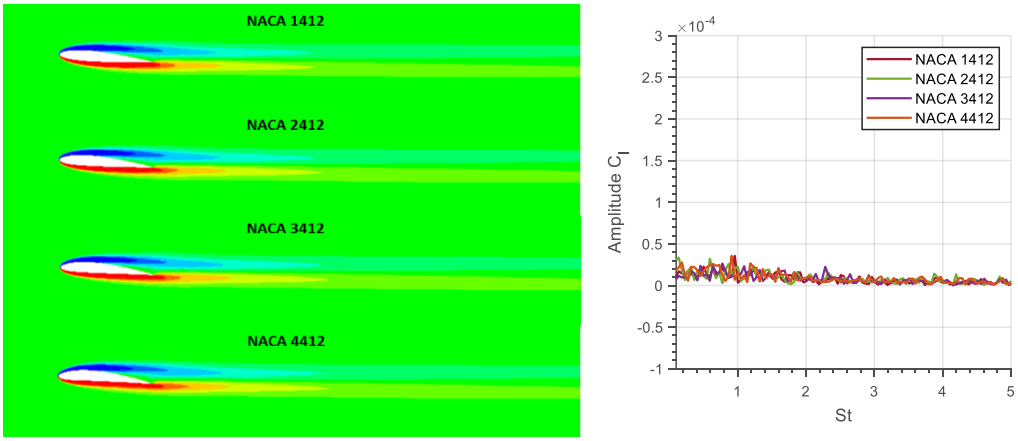

Figure 30: Instantaneous vorticity patterns for NACA1412, NACA2412, NACA 3412, and NACA4412 at α = 5° at t*=73.

However, NACA 4412 airfoil starts to generate oscillation at α = 6° where CW and CCW vortex structures are visualized at the wakefield (Figure 31). The continuous form of the upper vorticity field separates at around 2c distance at downstream, and the lower vorticity field separates at around 2.5c distance. Then both start to dissipate at further distances like around 3.5c. The generation of wakefield vortex formation can also be confirmed from the Strouhal number distribution where NACA 4412 airfoil shows a spike in lift coefficient spectrum with St = 0.867 where other airfoils do not show any spike at all. As the angle of attack increases to α = 7°, alternating vortex shedding patterns are more visible for NACA 4412 airfoil but other airfoils still do not show any vortex formation (Figure 32). The shapes of the vortices close to the airfoil change along with the wakefield distance. At a low Reynolds number like Re = 1000, two rows of vortices are formed, clockwise (CW) rotating upper row (blue in the figure) and counterclockwise (CCW) rotating lower row (red in the figure). At the same time, the Strouhal number distribution shows an amplitude rise for only NACA 4412 airfoil with St = 0.684, but other airfoils do not show any amplitude spectrum rise.

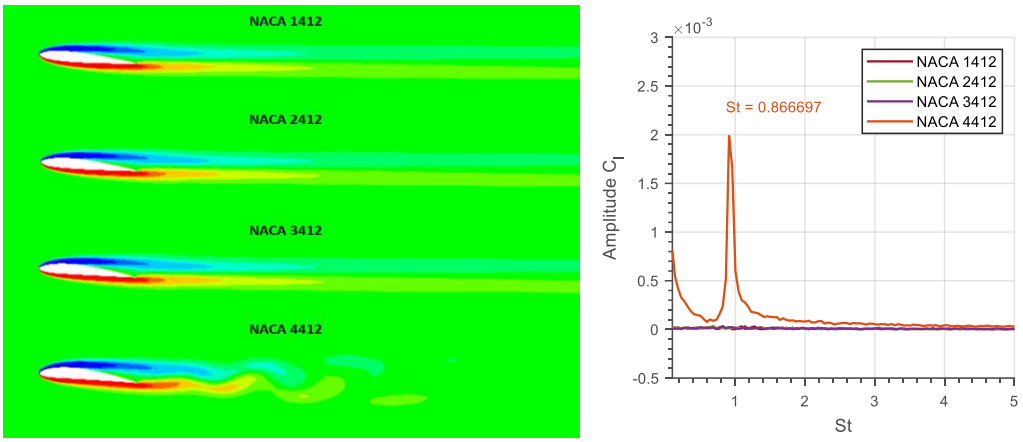

Figure 31: Instantaneous vorticity patterns for NACA1412, NACA2412, NACA 3412, and NACA4412 at α = 6° at t*=73.

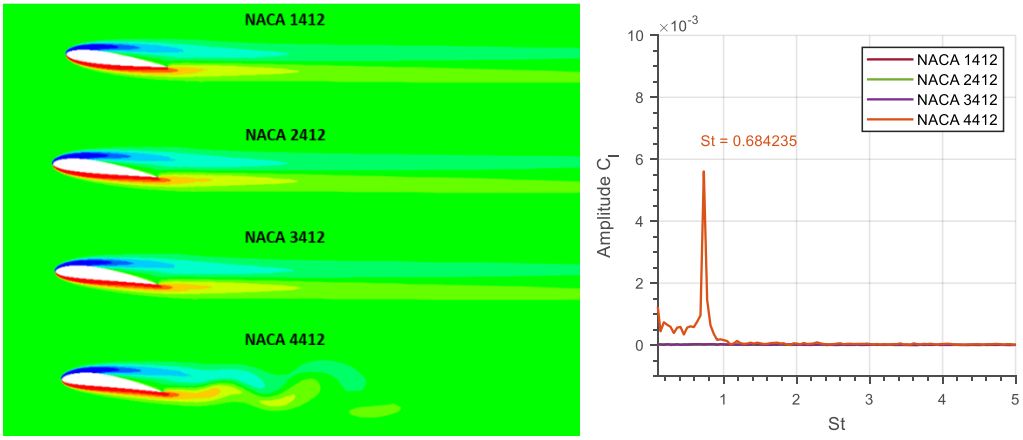

Figure 32: Instantaneous vorticity patterns for NACA1412, NACA2412, NACA 3412, and NACA4412 at α = 7° at t*=73.

At α = 8°, NACA 2412, NACA 3412, and NACA 4412 airfoils start to generate alternating vortices at the trailing edge of the airfoils (Figure 33). The shortest vortex detachment is seen from the NACA 4412 airfoil, and the longest is from the NACA 2412 airfoil. NACA 1412 airfoil does not show any vortex layer detachment. The width of the vortices also differs from airfoil to

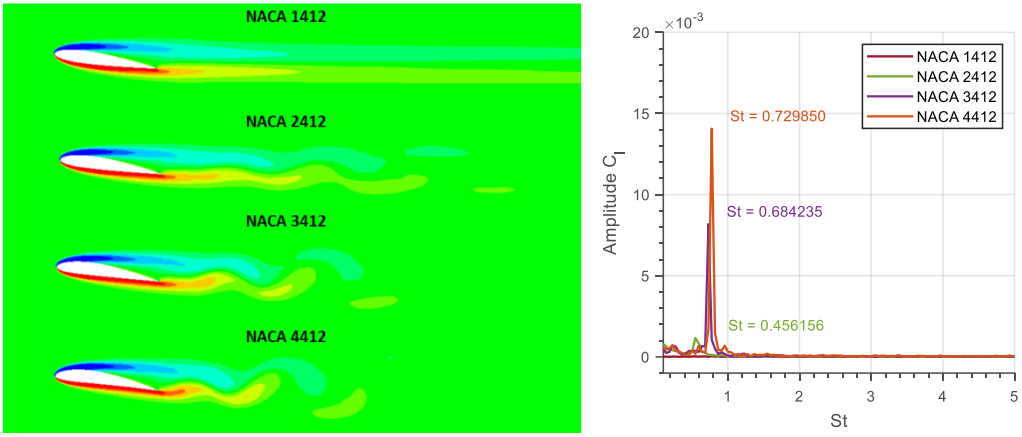

Figure 33: Instantaneous vorticity patterns for NACA1412, NACA2412, NACA 3412, and NACA4412 at α = 8° at t*=73.

airfoil. NACA 4412 which has the highest camber of those four airfoils, tends to have the fastest wakefield detachment. On the other hand, the lowest cambered airfoil NACA 1412 does not show any wakefield detachment at all. By looking at the lift amplitude spectrum at the right column, it can be observed that NACA 4412 has the highest amplitude rise with St = 0.729 and NACA 2412 has the lowest amplitude rise with St = 0.456. At higher angles of attack like at α = 9°, all four airfoils generate wakefield detachment, and as before NACA 4412 airfoil shows the fastest detachment, and the shapes of the vortices start to take droplet shapes. On the other hand, NACA 1412 demonstrates the slowest wakefield detachment among the four NACA airfoils. At the same time, the lift coefficient amplitude spectrum shows that NACA 4412 and NACA 3412 airfoils show the highest rises in amplitude with St = 0.821, and the lowest rise in amplitude is shown by NACA 1412 with St = 0.639. The shapes of the vortices become more like droplets at α = 10°, and wakefield detachment distances become significantly shorter. The wakefield detachment of NACA 1412 airfoil can be observed at a distance of x = 1.5c from the trailing edge of the airfoil where the wakefield detachment of NACA 4412 airfoil at x = 0.5c from the trailing edge. In addition, all the airfoils generate at least three couple of vortices (CW and CCW) until they dissipate. In all those cases, the upper row of the wakefield detaches faster than the lower row.

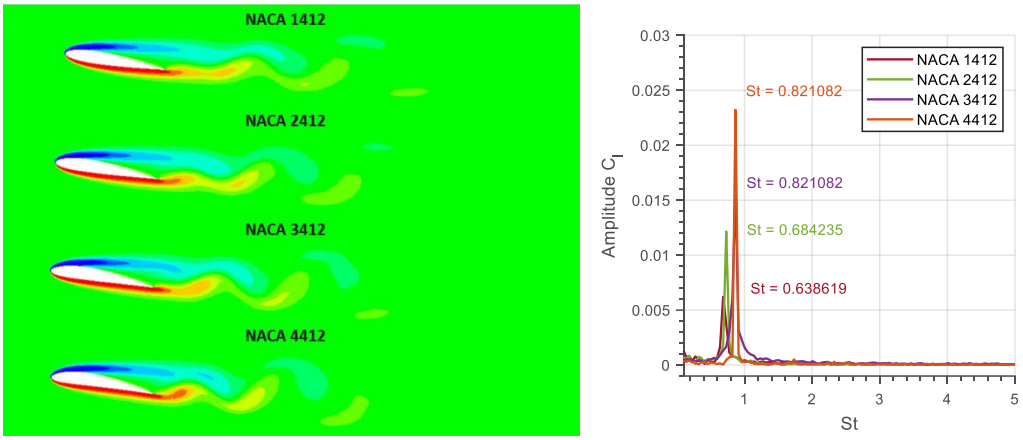

Figure 34: Instantaneous vorticity patterns for NACA1412, NACA2412, NACA3412, and NACA4412 at α = 9° at t*=73

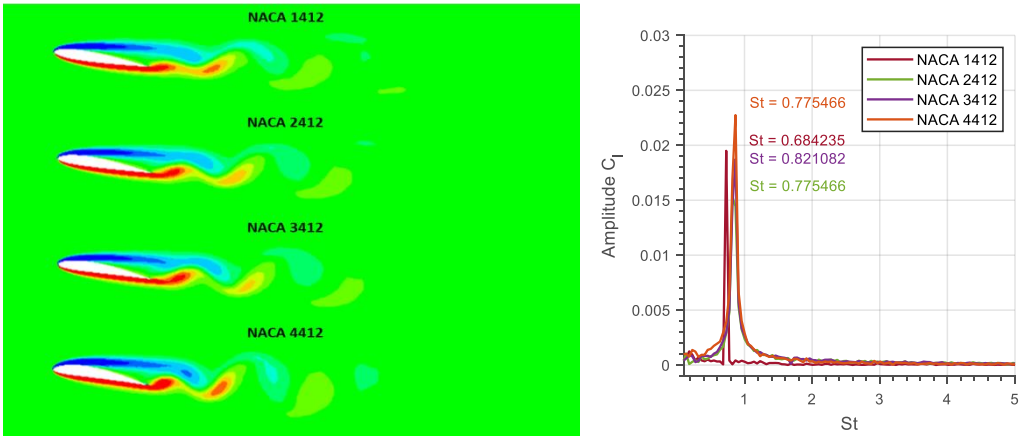

Figure 35: Instantaneous vorticity patterns for NACA1412, NACA2412, NACA3412, and NACA4412 at α = 10° at t*=73

In terms of lift coefficient amplitude spectrum, NACA 4412 airfoil demonstrates the highest rise with St = 0.775 however, NACA 3412 airfoil shows the highest Strouhal number (St = 0.821) even though the amplitude is less than the NACA 4412 airfoil. A clear correlation between the instantaneous aerodynamic force coefficients and the lift coefficient amplitude spectrum was visible from the previous chapter. At this stage, the correlation between the camber, the vortex pattern, and the lift coefficient amplitude spectrum can be observed. It can be concluded that as the camber of the airfoils increases the wakefield detachment and the vortex formation procedure become faster. At the same time, peaks in the lift coefficient amplitude spectrum

indicate that the specific airfoil starts to generate vortices in the wakefield. The longitudinal and lateral spacing of the vortices changes as the angle of attack changes. The vortices at the wakefield start to take droplet shapes after the detachment as the angle of attack increases. The same thing can be visible from the instantaneous lift coefficient amplitude spectrum as well. High amplitude values in the lift coefficient amplitude spectrum indicate a fully developed droplet-shaped vortex.

CHAPTER 4

COMPARISON BETWEEN 2D AND 3D SIMULATIONS OF NACA 4412

According to the previous studies, out of four 4-digit NACA airfoils, NACA 4412 produces the highest lift at a low Reynolds number like Re = 1000. Therefore, to investigate the flow behavior further, the 3D airfoil of NACA 4412 has been investigated at Reynolds number 1000 for angles of attack range starting from α = 0° to 10° as the purpose of the study is to find out whether the flow behaves in the same way as it did in 2D analysis. This chapter studies the 3D analysis on NACA 4412 airfoil under the same conditions as 2D analysis which has been discussed in the previous chapters. At the end of this chapter, a comparison study has been included to understand the flow behavior difference between the 2D and the 3D analyses.

4.1 Method and Geometry

The same cambered airfoil NACA 4412 has been used in this 3D study as it was used in the previous 2D analysis using Eq 3. This 3D simulation has been carried out at Reynolds number 1000 using the same boundary condition as it was in 2D analysis.

A grid generation software Pointwise has been used to generate mesh as the software gives full control of the grid node and element number. In that way, both the 2D and 3D cases could be prepared with almost the same accuracy in terms of node numbers, element numbers, boundary layer, etc. The mesh surrounding the airfoil consists of two regions: an inner region, and an outer region, where the inner region is an unstructured triangular grid mesh with a semi-circle shape with a radius of 2.5c with a center at c/4 location of the airfoil at the upstream and a rectangular region with a width of 2.5c at the downstream. The inner region starts right after the boundary layers and extends up to the outer region. A Total of 15 boundary layers have been

used in this simulation with an initial thickness of 0.025 mm growing with a rate of 1.1. the outer region is a C-type structured rectangular mesh with a radius of 25c and a rectangular design at the wake of the airfoil with a length of 30c. The downstream length of the domain is kept long so that the wake pattern can be observed clearly.

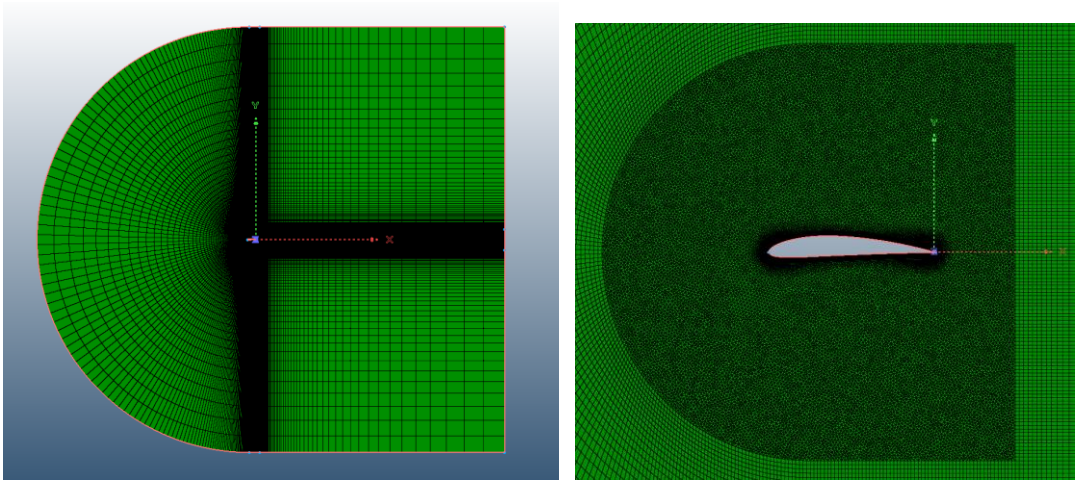

(a) Outer and inner mesh region

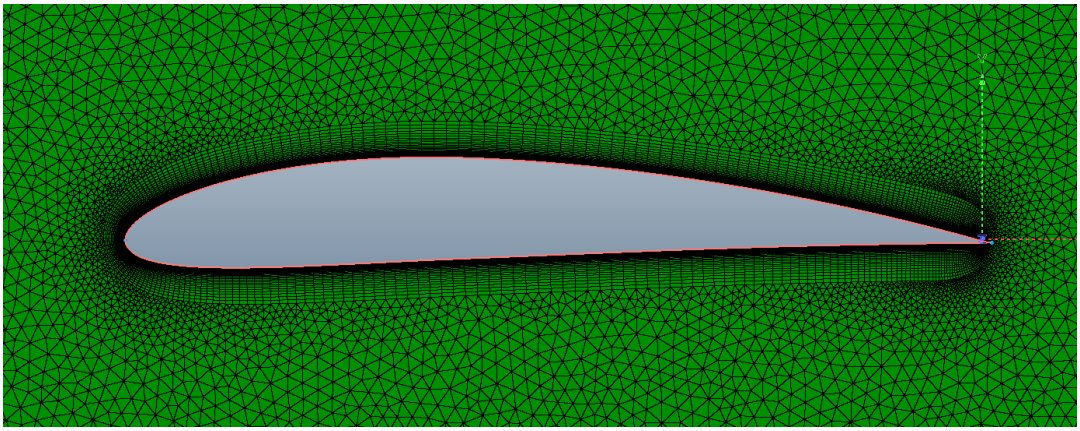

(b) Boundary layer around NACA 4412

Figure 36: Domain and mesh around NACA 4412 for simulation.

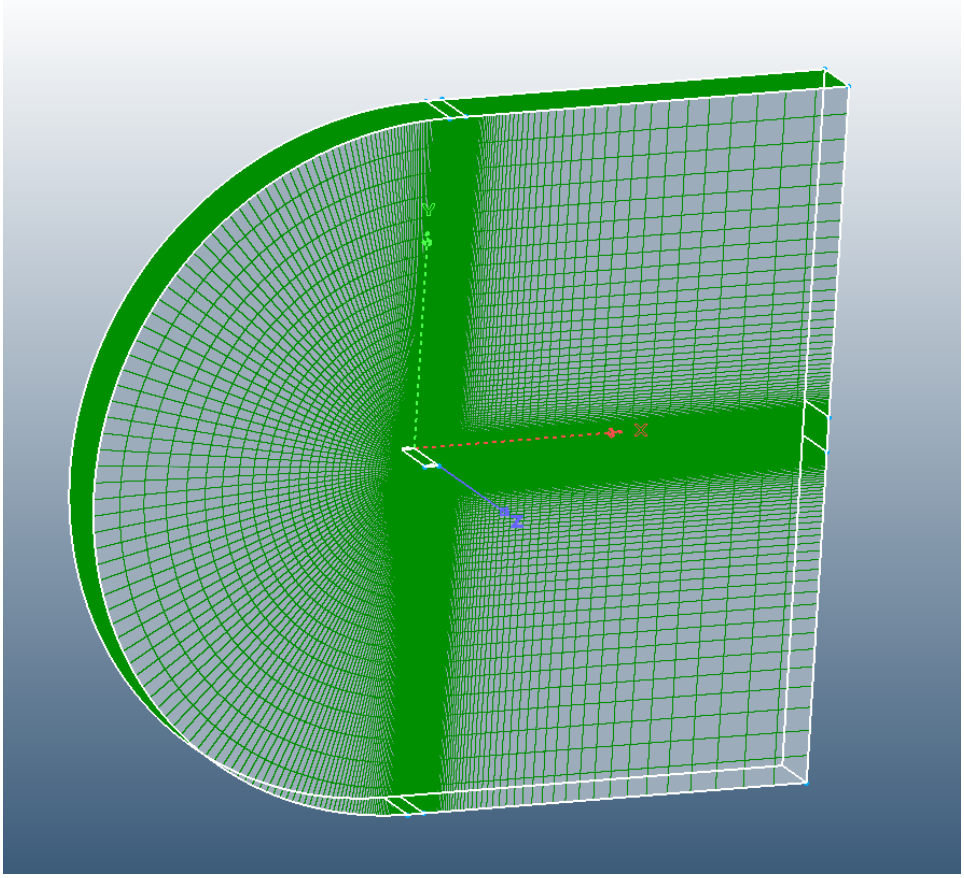

(a) Domain after extrusion in z-axis.

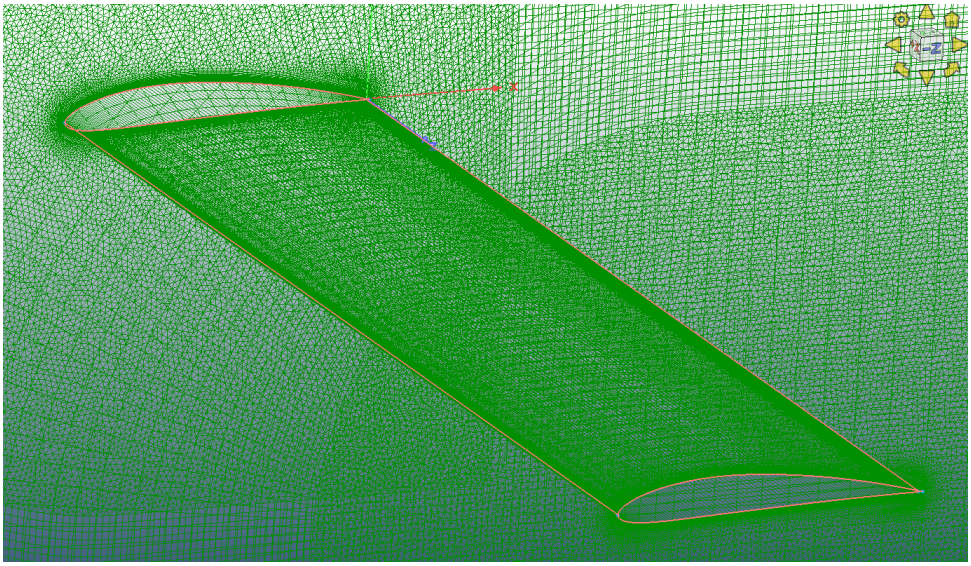

(b) 3D airfoil of NACA 4412 after extrusion

Figure 37: Domain and airfoil NACA 4412 after extrusion in z-axis.

The angle of attack is defined as positive in the clockwise direction starting from 0° to 10° with an increment of 1° per analysis. The pivot point for angles is located at the 0.25c point from the leading edge of each airfoil.

The whole mesh domain is then extruded in the z-axis direction by a length of 10 mm or 0.1c with 50 steps (Δz), meaning 0.2 mm per step. Therefore, the span of the wing is 0.1c or 10 mm and that results in 0.001 m2 as wing area = span x chord length. The 3D version of the domain mash and the airfoil are demonstrated in Figure 37.

The semi-circular region of the outer domain is used as the velocity inlet, and the other side of the outer region has been used as the pressure outlet. The external condition of the flow around all the airfoils is obtained for various angles of attack at Re = 1000.

ANSYS Fluent was used for simulating the flow which uses the finite-volume method in order to solve equations of conservative. [Ansys user manual].

During the analysis, the second-order implicit method has been used for the transient solution. A SIMPLE-type implicit algorithm is implemented for pressure-velocity coupling. The solution of the simulation is accurate by a second order in space and time.

The time increment used for this study is Δt = 0.005s. The simulations are conducted until t = 50 s and a non-dimensional time, $t* = \frac{t*U\infty}{c} = 73.05$ where the free stream velocity, Uinf = 0.146 m/s and chord length, c = 0.1 m. The computational time interval is t*ϵ [0 73.05] for the simulations. To observe the convergence of a flow t = 50 s is well enough. The results of the analysis and their discussions are documented below in detail to investigate the difference between 2D and 3D analyses.

4.2 Grid and Time Refinement Study

To proceed with the three-dimensional analysis, a detailed time and grid refinement study has been conducted on the 3D NACA 4412 airfoil. For grid refinement study, three different meshes: coarse, medium, and fine have been applied only for angle of attack 10°. For coarse mesh, the two-dimensional mesh domain (Figure 36 (a)) has been extruded toward the z-direction for 10 mm with 25 steps creating 0.4 mm extrusion per step. Similarly, for medium and fine mesh, same two-dimensional mesh domain has been extruded in the z-axis direction for 10 mm with 50 and 100 steps, respectively. That means, for medium and fine meshes, each step size is 0.2 mm and 0.1 mm, respectively. Total number of nodes and elements for each mesh are enlisted in Table 4. The time step used for the grid refinement study is, Δt = 0.005s and the simulations have been continued till t = 50 sec that is converted to a non-dimentional time value of, $t* = \frac{t*U\infty}{c}$ = 73.05 where the free stream velocity, Uinf = 0.146 m/s and chord length, c = 0.1 m using Ansys Fluent.

The main goal of this study is to investigate the aerodynamic behavior after the simulation results reach to steady-state condition which is periodic condition in this case. So, the early condition of the simulation results is ignored.

Table 3: Meshes of 3D NACA 4412 domains at α = 10°.

Meshes	**Nodes around the airfoil**	**Total number of Elements**
Coarse	1,531,920	1,931,250
Medium	3,004,920	3,862,500
Fine	5,950,920	7,725,000

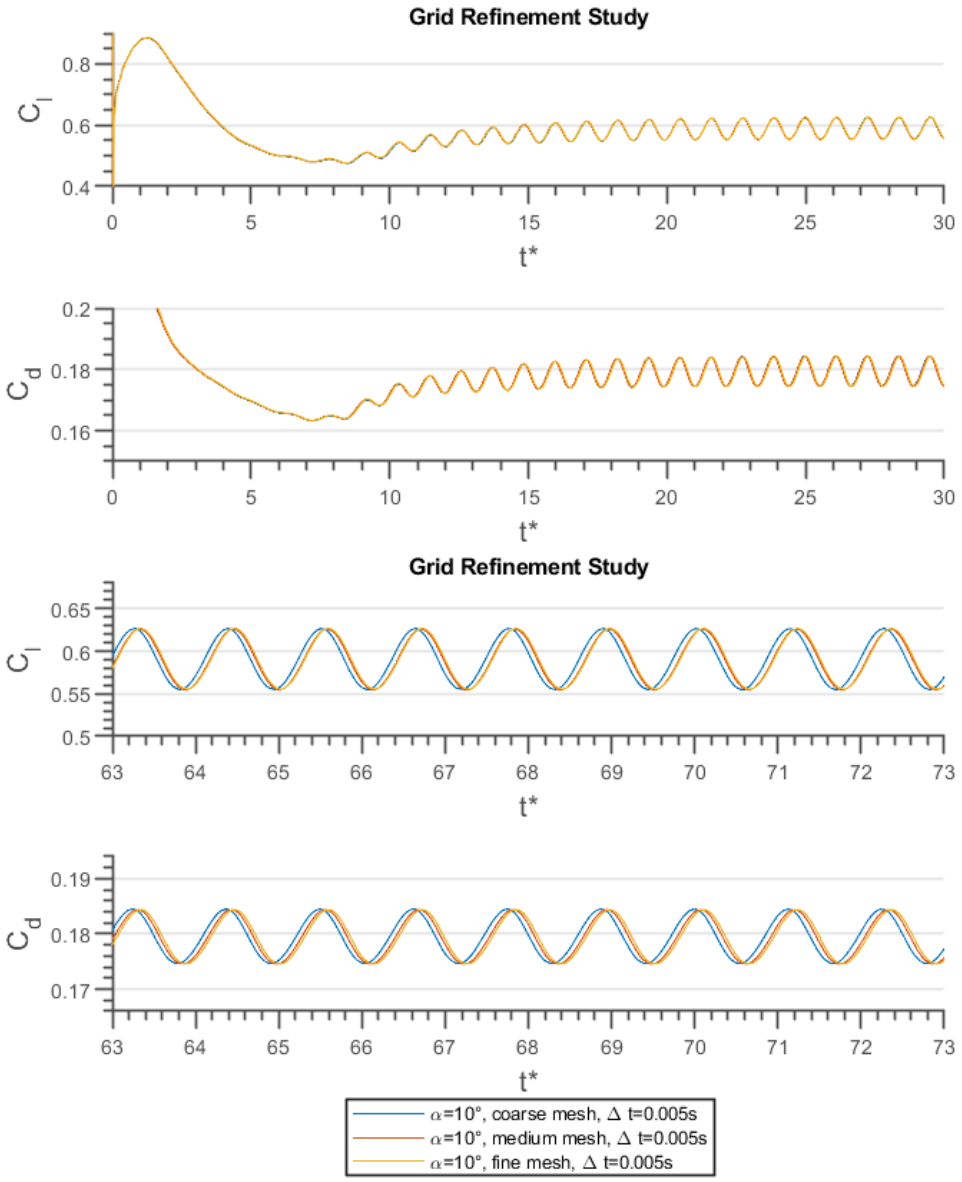

Figure 38: Instantaneous lift and drag coefficients from the grid refinement study during t*ϵ [0 30] (top two rows) and during t*ϵ [63 73] (bottom two rows) for α=10°.

Grid refinement study results are plotted in Figure 38 where instantaneous lift and drag coefficients for all three meshes start with an initial rise and then reach to a periodic oscillation condition after around t* = 22. From a close view, the coarse mesh generates results with a phase delay than the medium and fine meshes.

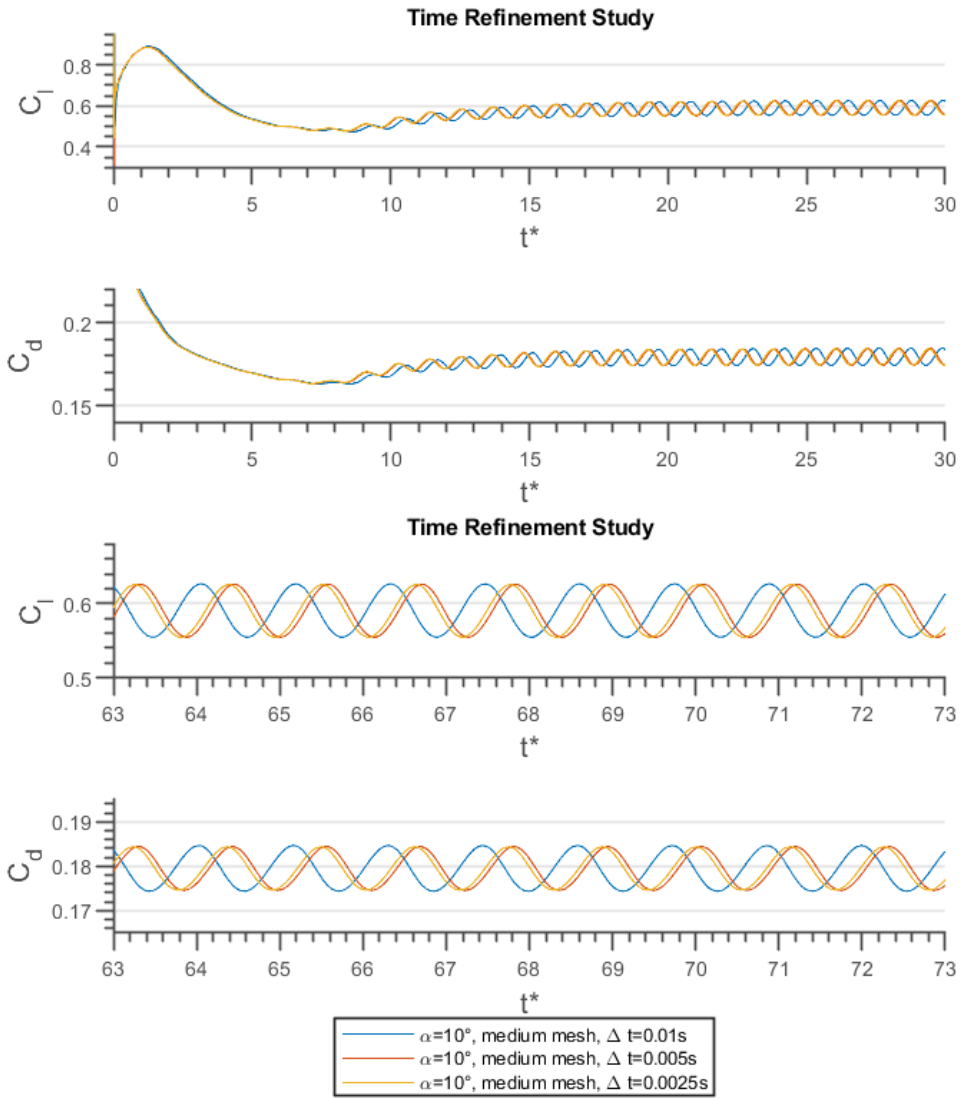

Figure 39: Instantaneous lift and drag coefficients from the time refinement study during t*ϵ [0 30] (top two rows) and during t*ϵ [63 73] (bottom two rows) for α=10°.

However, medium, and fine meshes show almost no difference in the periodic steady condition. Therefore, considering this condition the rest of the analyses have been conducted using medium mesh as the medium mesh consumes less simulation time.

In a similar way, a detailed time refinement study has been conducted using the medium mesh using three different time steps (Δt): 0.01s, 0.005s, and 0.0025s to see

how change in time steps change the overall aerodynamic behavior. The simulations are continued till non-dimensional time, t* = 73.05 (t = 50s) in Ansys Fluent.

Results from the time refinement study are plotted in Figure 39, where instantaneous aerodynamic coefficients for all three time steps initialize with a rise and then start to converge with a periodic oscillation starting from around t* = 22. At this steady periodic phase, time step 0.1s demonstrates a phase shift but keeping almost the same frequency and amplitude as the other two time steps. Time steps 0.005s and 0.0025s show very close results leaving almost negligible differences both in terms of amplitude and frequency. As a result, to same simulation time and cost, time step 0.005s has been used for the rest of the analyses.

4.3 Aerodynamic Coefficients Comparison

In this part, the aerodynamic results found from the 3D simulation are compared with the 2D simulation. Figure 40 shows the comparison between the 2D and 3D results of NACA 4412 for α = 0° at Re = 1000 where the blue line represents the 3D results and the red line represents the 2D results.

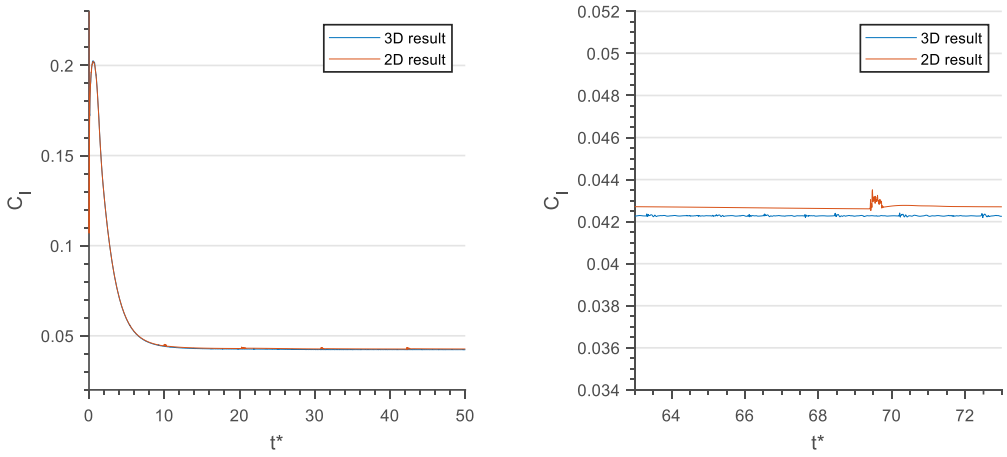

(a) Lift coefficient comparison between 2D and 3D results

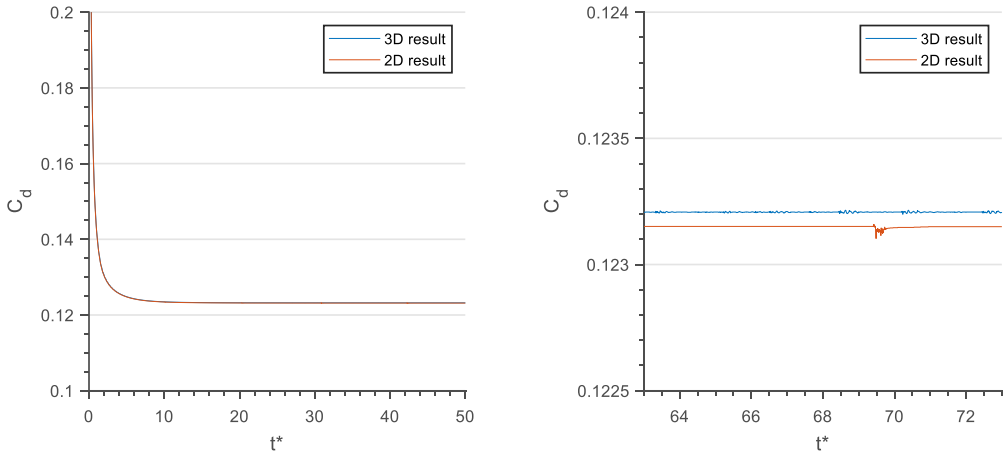

(b) Drag coefficient comparison between 2D and 3D results

Figure 40: Comparison of aerodynamic coefficients (cl and cd) at α = 0°.

In this figure, 2D and 3D results show almost no difference between them both in lift and drag coefficient distributions at α = 0°. In terms of convergence timeline, 3D

simulation results converge at the same time as the 2D simulation results at t* = 17 both in lift and drag coefficient plots.

In plot (a), at the initial phase of the 3D lift coefficient distribution, the results spike up to around 0.202 but then gradually converge down to 0.0425 at around t* = 17. Similarly, the 2D lift coefficient distribution results rise to around 0.202 and converge down to around 0.043 at about t* = 17. So, a slight difference of 0.0005 in converged value of lift coefficient is observed meaning 2D airfoil of NACA 4412 produces more lift at $\alpha = 0°$. Plot (b) shows a comparison of drag coefficient in between 2D and 3D results at $\alpha = 0°$. Both 2D and 3D drag coefficient results rise in a similar pattern and then converge down at around 0.123 for both cases at t* = 17 which is similar to the lift coefficient distribution in the plot (a). It should be noted that at this angle of attack of 5°, 3D simulation results of lift coefficient start to show oscillation however this oscillation can be neglected as the range in between upper and lower value is around 0.0001, which is negligible.

Figure 41 demonstrates the difference between the aerodynamic results of 2D and the 3D simulations at $\alpha = 5°$ for Re = 1000 to understand the lift and drag coefficient variation just before the oscillations start. Plot (a) provides the comparison in terms of lift coefficients, and plot (b) provides the comparison in terms of drag coefficients. In Plot (a), the lift coefficient value of both 2D and 3D simulation spike up to 0.536 and 0.538, and then converges down to 0.298 and 0.299 respectively, and they both converge at around t* = 16. Drag coefficient comparison in plot (b) shows that both 2D and 3D results startup with a high drag coefficient value, but both converge at around 0.134 at t* = 16.

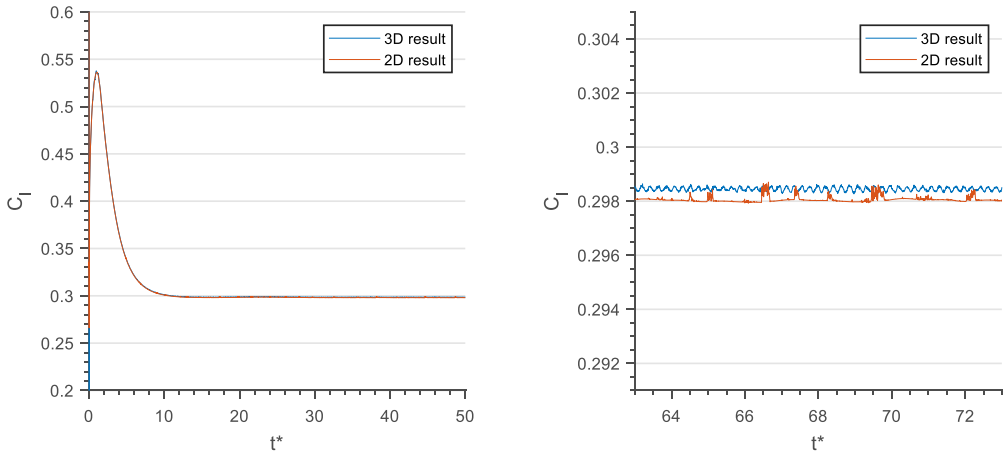

(a) Lift coefficient comparison between 2D and 3D results

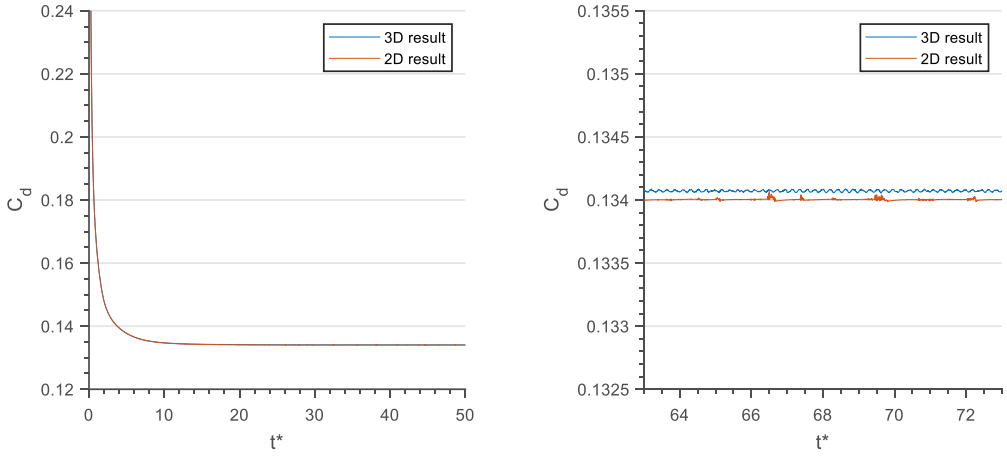

(b) Drag coefficient comparison between 2D and 3D results

Figure 41: Comparison of aerodynamic coefficients (cl and cd) at α = 5°.

To observe the dissimilarity between 2D and 3D results at the angle of attack where oscillations start, Figure 42 has been plotted for α = 6° at Re = 1000. Both lift and drag coefficient distributions are demonstrated in the plot (a) and plot (b) respectively.

From plot (a), the oscillation of 2D simulation starts from t* = 23 and keeps growing until t* = 63 and then continues to stay with the same upper and lower lift coefficient values of 0.354 and 0.347 respectively keeping a static value of 0.351. For 3D simulation results, the oscillation starts getting countable after t* = 33 and keeps

growing until t* = 64 and then stay constant with an upper and lower lift coefficient value of 0.346 and 0.342 respectively with a center static value of 0.344.

Therefore, at this angle of attack of 6°, the 2D airfoil produces a slightly higher lift than the 3D airfoil by approximately 0.01.

Same way, the drag coefficient distribution of 2D and 3D simulations are plotted in the plot (b) where the oscillation for 2D drag coefficient results starts to be countable after t* = 31 and grows by amplitude until t* = 50. After that, the oscillation stays with the same upper and lower drag coefficient values of 0.14 and 0.139, respectively, centering a constant value of 0.1395.

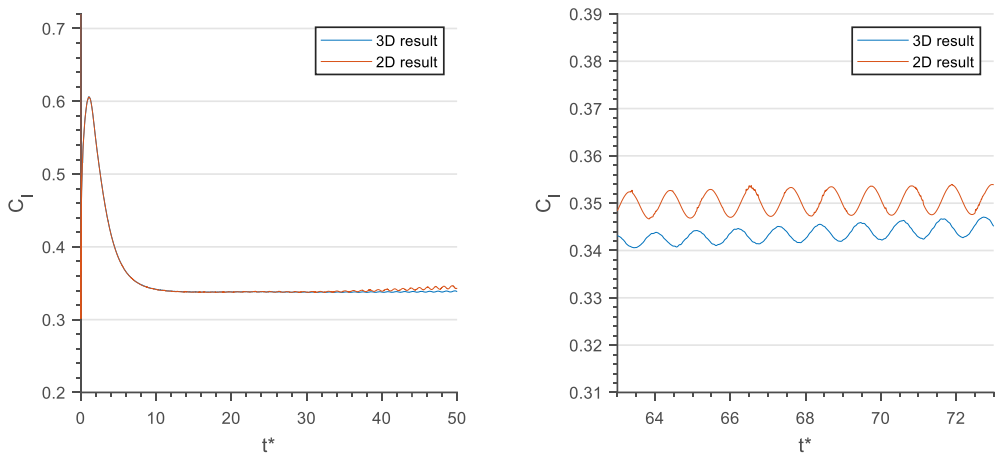

(a) Lift coefficient comparison between 2D and 3D results

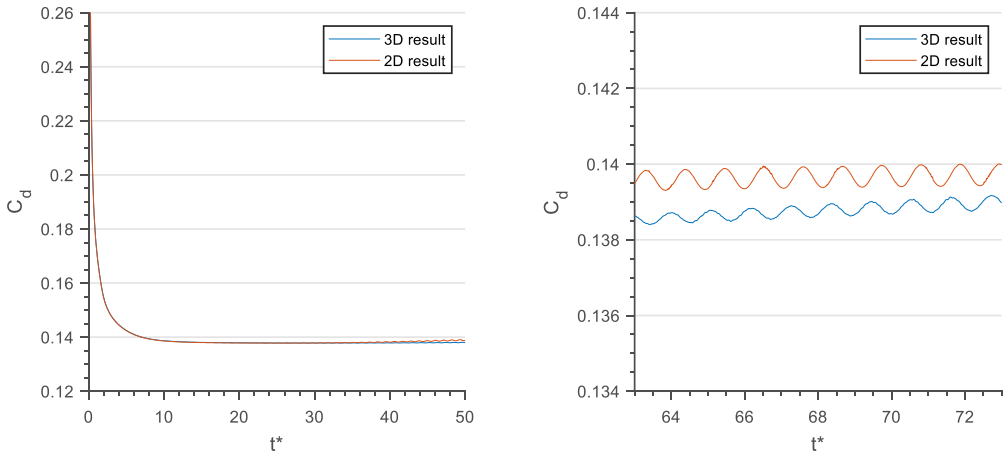

(b) Drag coefficient comparison between 2D and 3D results

Figure 42: Comparison of aerodynamic coefficients (cl and cd) at α = 6°.

A better understanding of the difference between 2D and 3D flow behavior can be grasped from Figure 43 and Figure 44 as these figures contain the simulations at higher angles of attack of 9° and 10° and with regular oscillation. Figure 43 shows the comparison in terms of lift and drag coefficients between 2D and 3D airfoil simulations at α = 9°. Plot (a) demonstrates the difference of lift coefficients between 2D and 3D simulations with respect to non-dimensional time, t*.

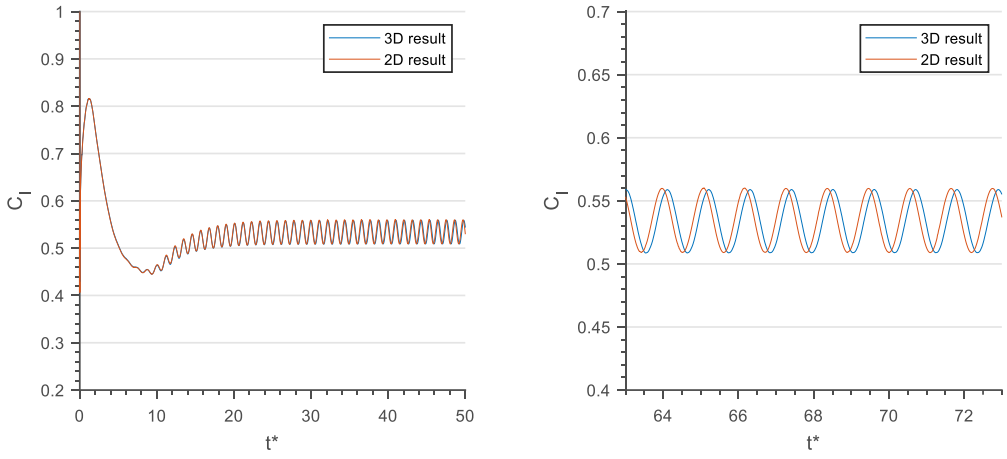

(a) Lift coefficient comparison between 2D and 3D results

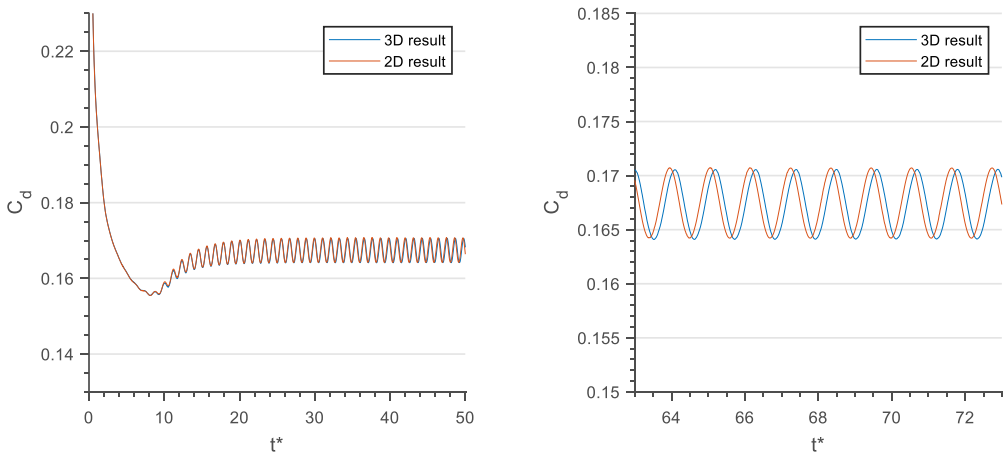

(b) Drag coefficient comparison between 2D and 3D results

Figure 43: Comparison of aerodynamic coefficients (cl and cd) at α = 9°.

Both results start with a high value but converge later with an oscillation around a static value of 0.535, which is expected at higher angles of attack. For NACA 4412, this oscillation is seen to be starting at α = 6° and continues to grow larger at angles

of attack higher than α = 6°. Both 3D and 2D results show a high initial spike and then settle down oscillating with an upper and lower lift coefficient value of 0.56 and 0.51, respectively which means the oscillation centers at around 0.535. One point should be noted that the 2D simulation lift coefficient distribution has a slightly higher upper value and a slightly lower value in an oscillating wave. However, as the difference is very less, they have not been taken into account for this discussion. There is no notable difference in terms of convergence timeline as they both start converging at t* = 32 and continue to stay in that upper and lower value range for the rest of the simulation.

Plot (b) shows the comparison between 2D and 3D simulations in terms of drag coefficient at α = 10°. Here both 2D and 3D results settle down at around t* = 21 showing almost no significant difference in convergence timing. Both results converge to a certain static value and continue to oscillate around that center value. The difference between 2D and 3D drag coefficient results are very small and thus can be negligible. Both 2D and 3D drag coefficient results oscillate at around 0.167 with an upper and a lower lift coefficient value of 0.17 and 0.164 respectively. These upper and lower values stay within that range for the rest of the simulation.

A comparison between 2D and 3D simulations at an angle of attack of 10° is shown in Figure 44. Plot (a) demonstrates the lift coefficient difference between 2D and 3D simulations with non-dimensionalized time, t*. At the initial phase of the simulation, both 2D and 3D results rise up to 0.885 and then start to fall down until they start converging. Both 2D and 3D results start converging at around t* = 33 oscillating with an upper and lower lift coefficient value of 0.625 and 0.555 respectively centering around 0.59. although there is a slight difference between 2D and 3D simulation results, they are neglected as the difference is insignificant.

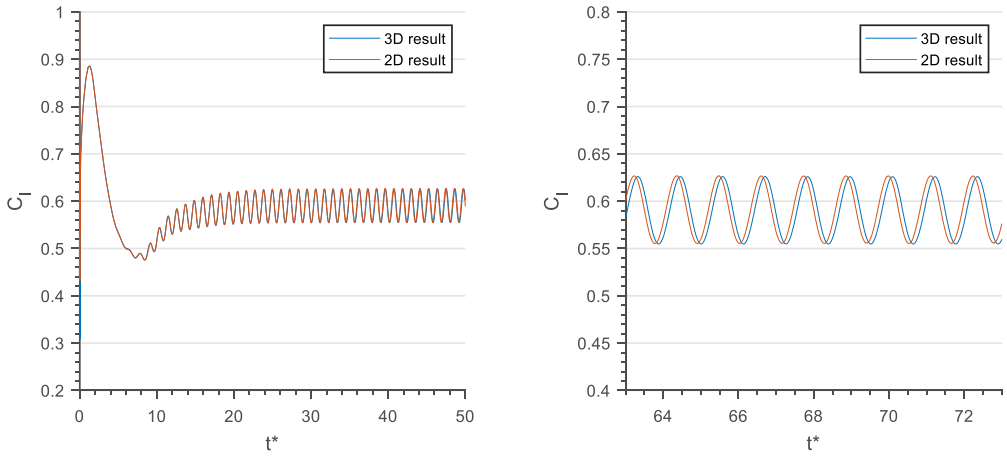

(a) Lift coefficient comparison between 2D and 3D results

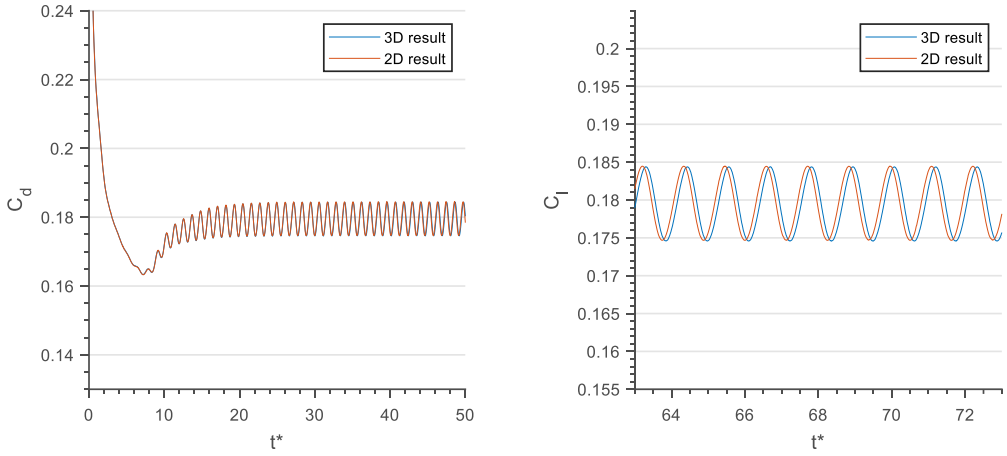

(b) Lift coefficient comparison between 2D and 3D results

Figure 44: Comparison of aerodynamic coefficients (cl and cd) at α = 10°.

Plot (b) represents the difference between 2D and 3D simulations in terms of drag coefficient at α = 10°. In this figure, both the 2D and 3D results spike up and converge with oscillations around a certain center drag coefficient value. 2D and 3D results both converge at around t* = 20.5 with an oscillation that has an upper and lower drag coefficient value of 0.184 and 0.175, respectively centering at around 0.18 where 2D results converge at around t* = 31 with an oscillation that has an upper and lower drag coefficient value of 0.182 and 0.171, respectively centering at around 0.178.

Table 1 shows the comparison of mean aerodynamic coefficients in between 2D and 3D simulations for various angles of attack. Two-dimensional results demonstrate slightly higher lift and drag forces than the three-dimensional simulation. For instance, at α = 10°, the differences between 2D and 3D results in terms of lift and drag coefficients are 0.1% and 0.06%, respectively.

Table 4: Comparison of mean aerodynamic coefficients for NACA 4412 2D and 3D simulations at α = 0° to 10°.

$\boldsymbol{\alpha}$	$\overline{C_l}(2D)$	$\overline{C_l}(3D)$	$\overline{C_d}(2D)$	$\overline{C_d}(3D)$	$\overline{C_l}/\overline{C_d}\,(2D)$	$\overline{C_l}/\overline{C_d}\,(3D)$
0°	0.0427	0.0423	0.1232	0.1232	0.3466	0.3433
1°	0.0986	0.0986	0.1242	0.1242	0.7939	0.7939
2°	0.1564	0.1567	0.1258	0.1259	1.2432	1.2446
3°	0.2062	0.2068	0.1280	0.1280	1.6109	1.6156
4°	0.2464	0.2568	0.1307	0.1308	1.8852	1.9633
5°	0.2922	0.2985	0.1340	0.1341	2.1806	2.2260
6°	0.3498	0.3428	0.1396	0.1387	2.5057	2.4715
7°	0.4151	0.4144	0.1478	0.1477	2.8085	2.8057
8°	0.4744	0.4741	0.1570	0.1570	3.0217	3.0197
9°	0.5346	0.5338	0.1675	0.1673	3.1916	3.1907
10°	0.5904	0.5898	0.1795	0.1794	3.2891	3.2876

In this section, the difference between 2D and 3D simulations in terms of aerodynamic coefficients especially, lift and drag coefficients are discussed and analyzed. Five angles of attack positions; 0°, 5°, 6°, 9°, and 10° have been mentioned here as those angles play a significant role in understanding the difference between 2D and 3D simulation results. In all those cases, 2D airfoil provides slightly higher lift and drag forces than 3D airfoil.

4.4 Pressure Distribution Comparison

To analyze the aerodynamic forces further, instantaneous pressure distributions are presented in this section. Only higher angles of attack; 9° and 10° are discussed as at those angles the airfoil shows the obvious characteristics of unsteady behavior.

Figure 43 shows the comparison between 2D and 3D simulation results in terms of pressure coefficient with respect to airfoil x-coordinate at $\alpha = 9°$. Both 2D and 3D results show a similar pattern where suction pressure on the upper surface increases for both the leading edge and trailing edge.

From the figure, it can be seen that the suction pressure on the upper surface in 3D simulation is a little bit higher than the 2D simulation results. At the same time, trailing edge pressure rises more than 2D which results in generating higher lift than 2D airfoil.

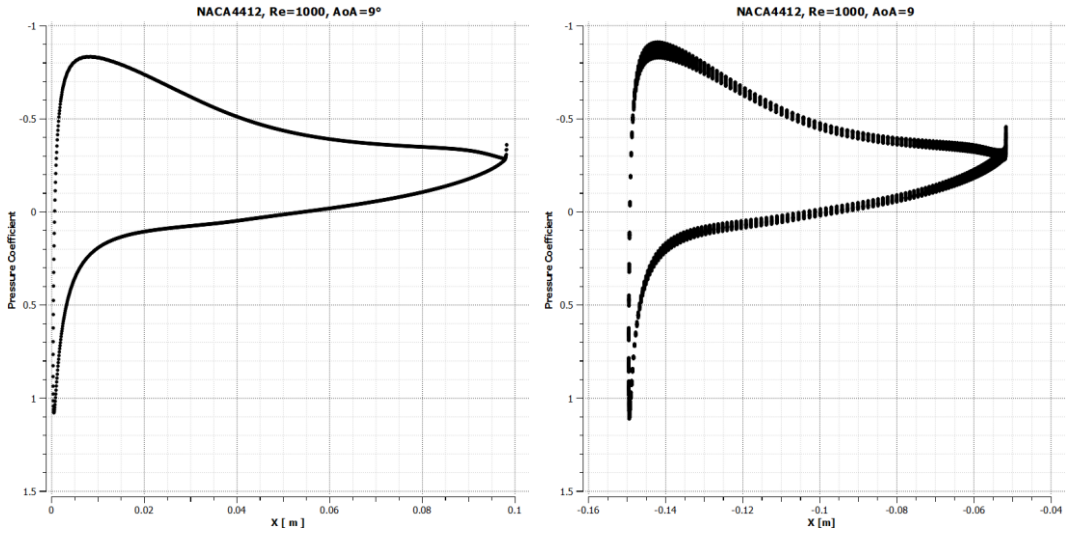

(a) Pressure distribution in 2D (b) Pressure distributin in 3D

Figure 45: Pressure distribution difference in 2D and 3D simulation on NACA 4412 airfoil at $\alpha = 9°$.

Pressure distribution comparison between 2D and 3D simulations around the airfoil at $\alpha = 10°$ can be observed in Figure 45. 3D simulation result produces higher suction pressure on the upper surface of the airfoil as well as a trailing edge. 3D results are

obtained using an average pressure value along the span of the wing, which can be seen in plot (b).

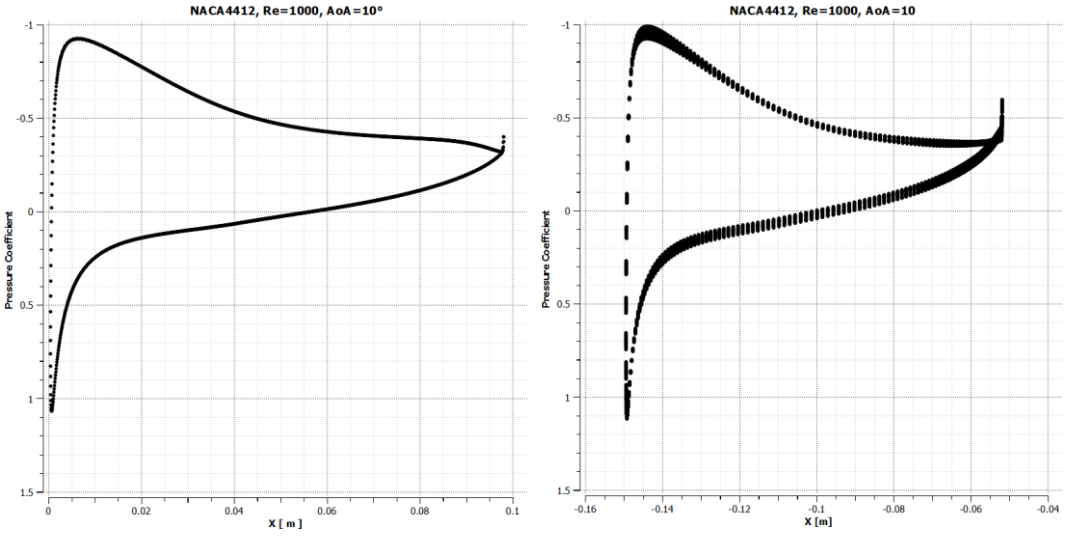

(a) Pressure distribution in 2D (b) Pressure distributin in 3D

Figure 46: Pressure distribution difference in 2D and 3D simulation on NACA 4412 airfoil at $\alpha = 10°$.

Pressure distribution changes slightly when the simulations are conducted on a 3D airfoil. From the study, it can be deduced that the suction pressure on the upper surface and at the trailing edge increases by an increasing angle of attack.

4.5 Skin Friction Coefficient Comparison

At low Reynolds numbers, the unsteady viscous flow tends to separate from airfoil more often than at high Reynold numbers. Due to this low Reynolds number, boundary layer thickness on airfoil becomes thicker, and frequent flow separation may occur. Therefore, the study of flow separation at low Reynolds numbers is critical to understanding the flow behavior.

In the following two figures, the difference between 2D and 3D simulation results in terms of skin friction coefficient are presented for $\alpha = 9°$ and $10°$ for Re = 1000.

Flow separation occurs when the skin friction coefficient value is zero meaning, there is no attachment on the surface of the airfoils.

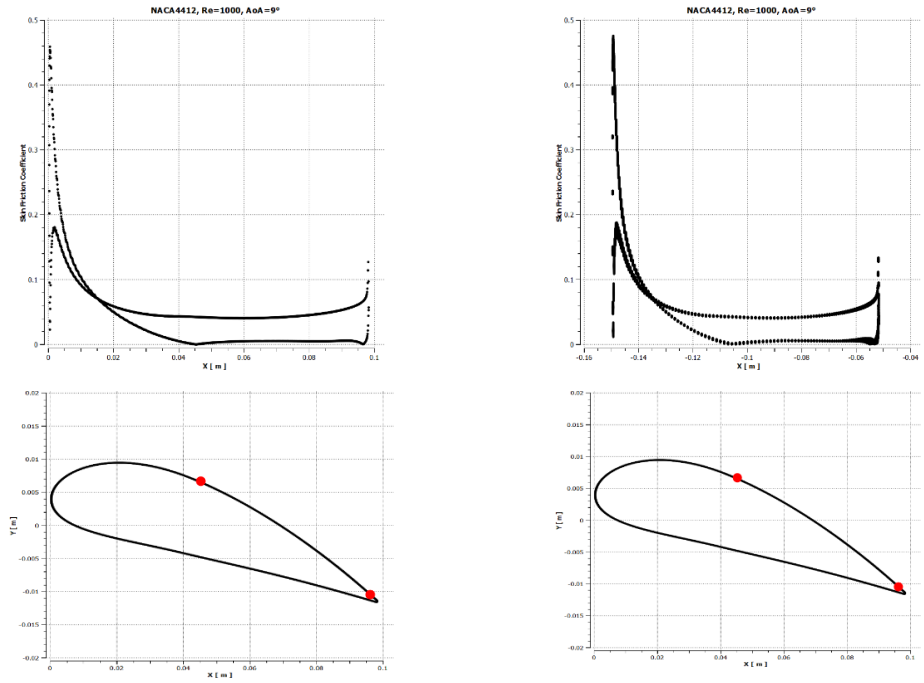

(a) 2D airfoil result (b) 3D airfoil result

Figure 47: Skin friction coefficient and relevent separation points on both 2D and 3D NACA 4412 airfoils at α = 9°.

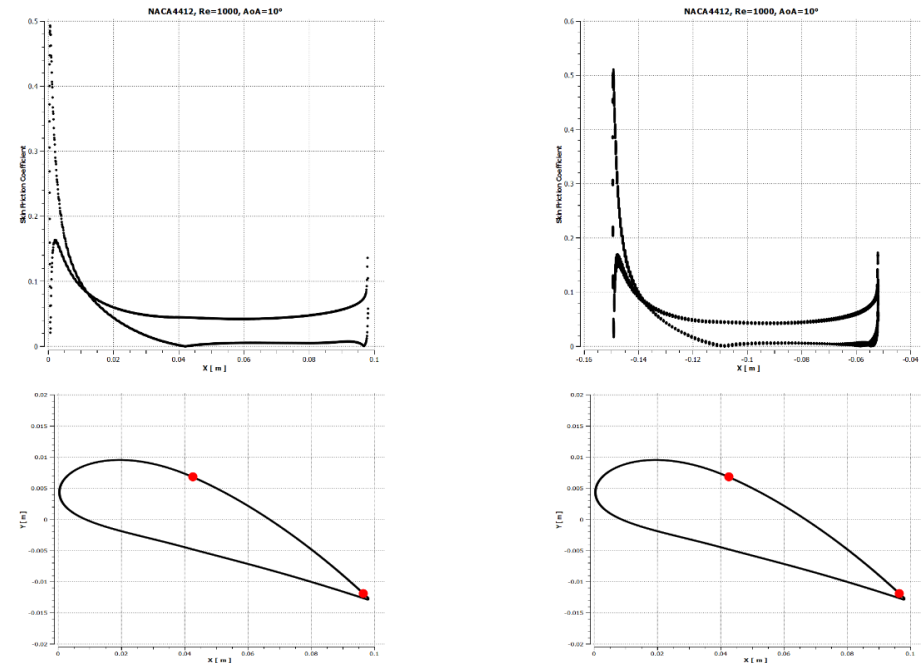

(a) 2D airfoil result (b) 3D airfoil result

Figure 48: Skin friction coefficient and relevent separation points on both 2D and 3D NACA 4412 airfoils at α = 10°.

The figures above indicate that both 2D and 3D simulations provide the same flow separation points on airfoil x-coordinate locations. Reattachment points on both 2D and 3D airfoils are the same as well. The separation points are pointed out on the airfoil schematic right under each skin friction distribution figure.

Flow separation differs hugely by the angle of attack, camber, maximum camber location, and thickness of airfoil. Here the angle of attack and camber plays the the biggest role in terms of flow separation. As the angle of attack increases, the flow separation point moves forward to the leading edge. On the other hand, as the camber increases, the flow separation points move back toward the trailing edge.

4.6 Strouhal Number Comparison

Amplitude spectrums of lift coefficients of both 2D and 3D NACA 4412 airfoils have been obtained for α = 5°, 6°, 7°, and 10° using Fast Fourier Transform (FFT). The lift coefficient starts oscillating after α = 6°. Therefore, to be certain angles of attack of 5°, 6°, 7°, and 10° are plotted in Figure 49. To avoid the initial errors of the computations, data from 51.1<t*<73 has been applied for the amplitude spectrum calculation.

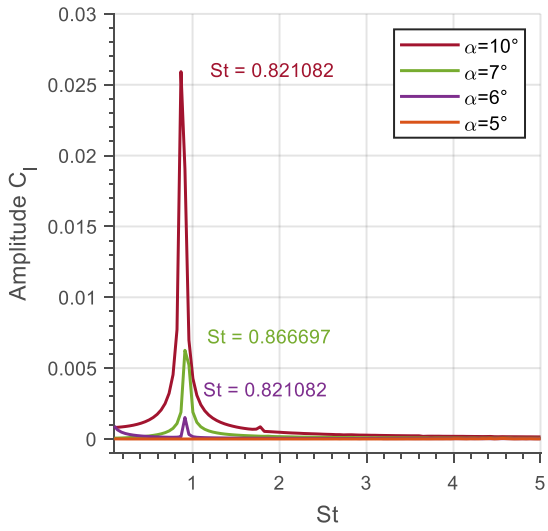

Figure 49: Amplitude spectrum of NACA 4412 at α = 0°, 5°, 7°, and 10° for 51.1<t*<73.

In the three-dimensional simulation, NACA 4412 airfoil starts forming vortices at α = 6° with St = 0.82 (Figure 49) with an amplitude of 0.0015. For higher angles of attack at α = 10°, the Strouhal number is also 0.82 but with an amplitude of 0.026. From Figure 49, it can be observed that there is no Strouhal number spike before α = 6°. At α = 7°, the Strouhal number increases to 0.87 with a lift coefficient amplitude of 0.006.

For further understanding, the amplitude spectrum of the three-dimensional results is compared with the two-dimensional results (right column) along with the lift coefficients of both results (left column) for α = 6°, 7°, 8°, 9°, and 10° in Figure 50. For a lower angle of attack α = 6°, where the oscillations started for NACA 4412 airfoil, the results from the 2D simulation data show higher results in both Strouhal number (St = 0.87) and amplitude (0.002). On the other hand, 3D results show a slightly lower value in both Strouhal number (St = 0.82) and amplitude (0.0015). The difference in values between 2D and 3D results can be justified by looking at the lift coefficient distribution in the left column, where the lift coefficient distribution from 2D simulation has higher frequency and amplitude than the 3D results.

At α = 7°, this difference between 2D and 3D results starts to close up but still contains a phase difference in the wave pattern. At this point, the Strouhal number of 2D and 3D results are St = 0.91 and St = 0.87, respectively. However, the amplitudes are almost similar for these two results having a slight difference of 0.0003. In the case of α = 8°, both the 2D and the 3D results have the same Strouhal number of 0.87, and in this case, the lift coefficient distributions oscillate with the same amplitude and frequency but have a slight phase-out.

α = 6°

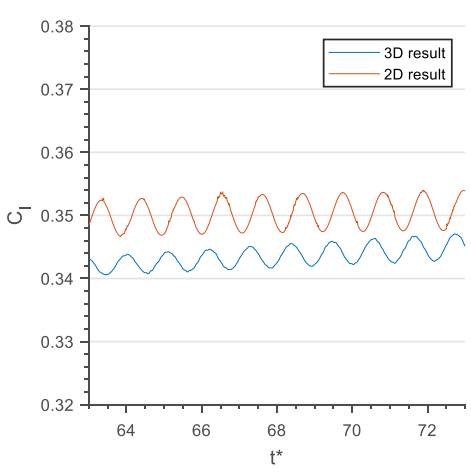
3D result
2D result
C_l
t*

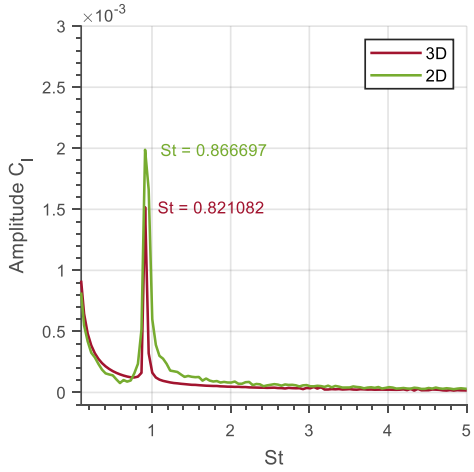
×10^-3
3D
2D
St = 0.866697
St = 0.821082
Amplitude C_l
St

α = 7°

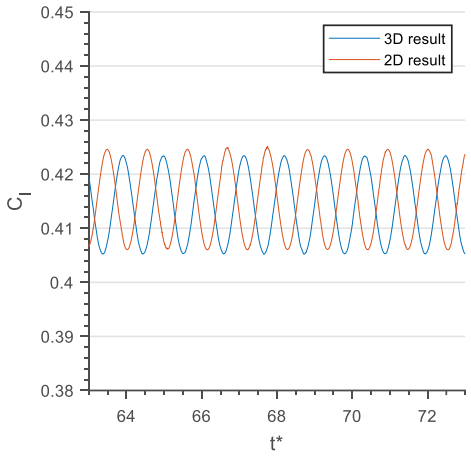
3D result
2D result
C_l
t*

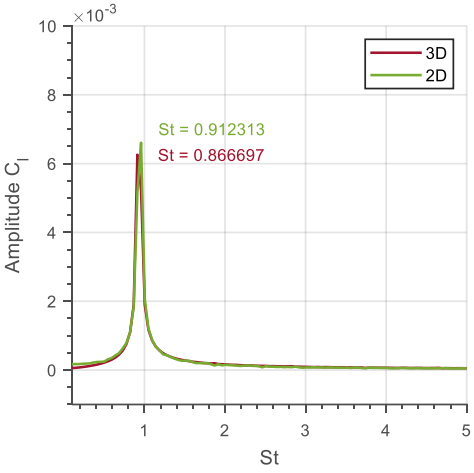
×10^-3
3D
2D
St = 0.912313
St = 0.866697
Amplitude C_l
St

α = 8°

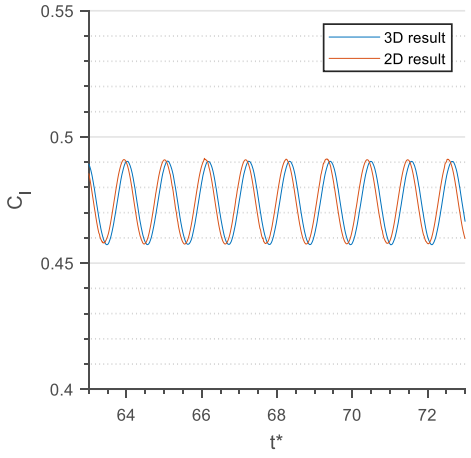
3D result
2D result
C_l
t*

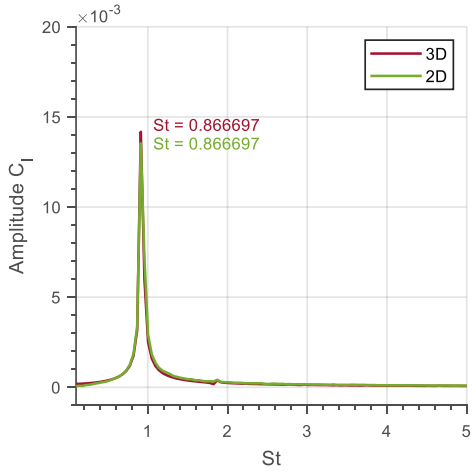
×10^-3
3D
2D
St = 0.866697
St = 0.866697
Amplitude C_l
St

α = 9°

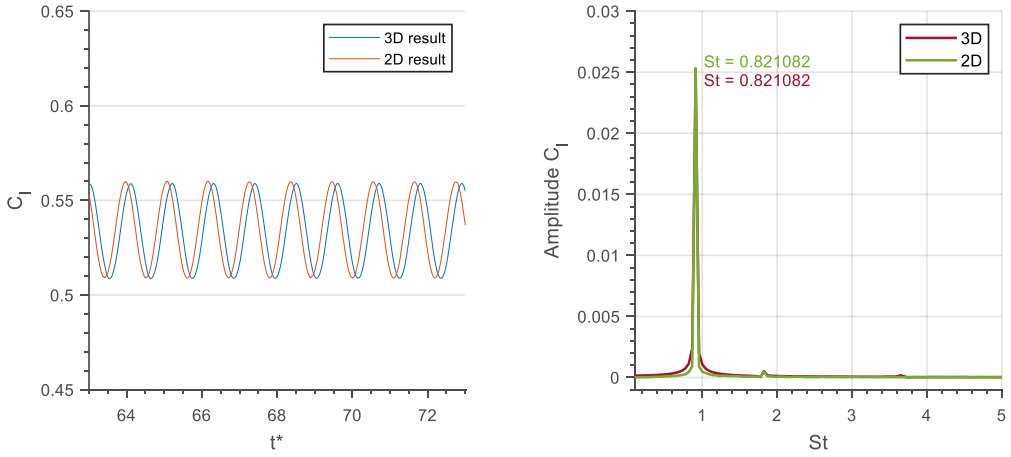

α = 10°

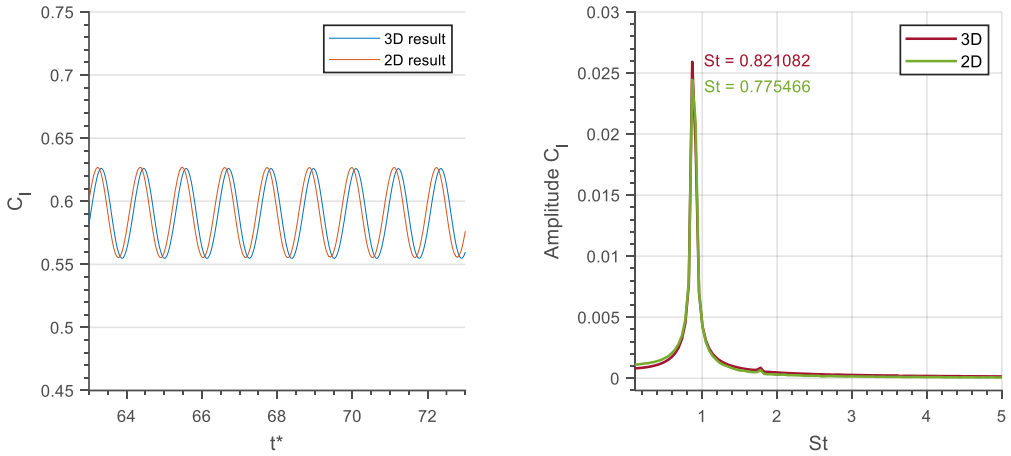

Figure 50: Correlation between lift-coefficient distribution (left column) and Strouhal number (right column) of 3D and 2D analyses of NACA 4412 airfoil at α = 6°, 7°, 8°, 9°, and 10° at Re = 1000.

At higher angles of attack at α = 9°, the Strouhal number of 2D simulations is the same as the 3D simulation data (St = 0.82). However, α = 10°, the Strouhal number of 2D simulation (St = 0.78) is lower than the 3D simulation data (St = 0.82). Lift coefficient distributions from both of these angles indicate that both 2D and 3D results have a similar lift coefficient distribution.

Table 5: Comparison between 2D and 3D simulations in terms of mean Cl, mean Cd, and Strouhal number for angles of attack of 6°, 7°, 8°, 9°, and 10° for Re = 1000.

$\boldsymbol{\alpha}$	$\overline{\boldsymbol{C}}_{\boldsymbol{l}}(\boldsymbol{2D})$	$\overline{\boldsymbol{C}}_{\boldsymbol{l}}(\boldsymbol{3D})$	$\boldsymbol{S_t}(\boldsymbol{2D})$	$\boldsymbol{S_t}(\boldsymbol{3D})$
6°	0.3498	0.3428	0.867	0.821
7°	0.4151	0.4143	0.912	0.867
8°	0.4744	0.4741	0.867	0.867
9°	0.5346	0.5338	0.821	0.821
10°	0.5904	0.5898	0.775	0.821

A table (Table 3) is prepared to understand the comparison between the 2D and 3D results all at once. It can be seen that the lift coefficients of the 2D simulation are slightly higher than the 3D simulation. On the other hand, the Strouhal numbers of the 2D simulation are also higher than the 3D simulation. However, they do not follow the same pattern after α = 9°.

4.7 Vortex Shedding Patterns

To assess and predict the vortex shedding phenomena in the wakefield of flapping wings, a good understanding of unsteady aerodynamic behavior at the wakefield of different airfoils at low Reynolds number flight regime at differenct angles of attack is necessary. However, to fully develop the knowledge of unsteady aerodynamics behavior, a progessive fundamental knowledge buildup is important starting from airfoil aerodynamic behavior at steady condition. Relative relations like Cl-α, Cl-Cd can be helpful for understanding perching, or flapping motions of airfoils at different angles of attack (Platzer & Jones, 2006). Several significant studies on unsteady aerodynamic behavior have been conducted on various airfoils so far. A detailed two-dimensional study on lift, drag, and pitching moment properties of NACA 0012 airfoil at low Reynolds number of 1000 for different angles of attack with a range of 0° to 90 °has been conducted by Kurtulus (Kurtulus, 2015). A later comparison study by Kurtulus (Kurtulus, 2016) on the unsteady flow pattern in the wakefield between NACA 0002, and NACA 0012 at low Reynolds number (Re = 1000) for angles of

attack starting from 0° to 180° gave a very good idea of how the vortices form in the wakefield of symmetric airfoils. A hybrid technique using both direct numerical simulation (DNS) and particle tracking velocimetry (PTV) was developed by Suziki(Suzuki et al., 2009; Suzuki T. & Yamamoto, 2009) to inspect the flow pattern of NACA 0012 airfoil starting at two different low Reynolds numbers (Re = 1000 and Re = 1300) up to a high Reynolds number (Re = 10,000) for angle of attack α = 15°. Not only two-dimensional but also three-dimensional cases are investigated by several authors. A study on the asymmetric wakefield structure at high angles of attack for 3D NACA 0012 airfoil at Re = 1000 by using direct numerial simulation (DNS) method was conducted by Kourser et al. (Kouser et al., 2021) to make a comparison between 2D and 3D flow behavior.

As a continuation of the previous progressive studies, the unsteady flow behavior at low Reynolds number for cambered airfoil is investigated in this chapter. In this section, z-vorticity of flow is shown and discussed for 3D simulation at six different angles of attack: 5°, 6°, 7°, 8°, 9°, and 10°. Each vortex pattern has been demonstrated as isometric view (left) and top view (right) to understand whether the vortex pattern changes spanwise for the 3D airfoil of NACA 4412. At low Reynolds number (i.e., Re = 1000) the vortices generate two rows of vortices: an upper and a lower vortex. The upper vortex row has a clockwise direction (CW) which is presented with blue color in the figures. The lower vortex row rotates at counterclokwise direction (CCW) that is shown with red color in the figures.

From Figure 51, it can be observed that an oscillation pattern formation occurs starting from an angle of attack of 6° at the wake of the airfoil, and this angle of attack can be considered as the critical angle where laminar flow faces its transition.

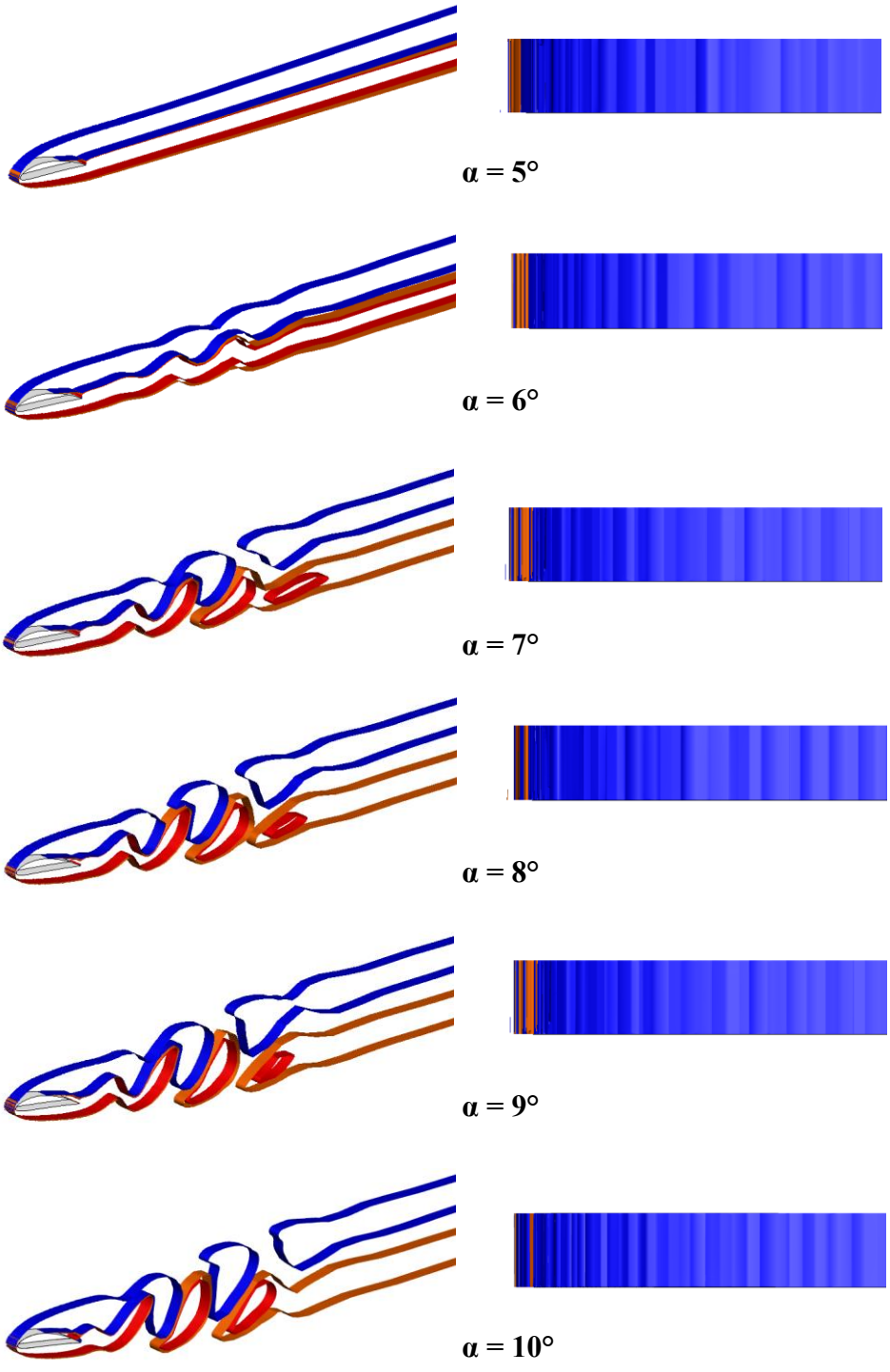

Figure 51: Vortex shedding pattern change of 3D NACA 4412 airfoil with progressive angle of attack from 0° to 10° at Re = 1000.

At α = 7°, the wakefield detachment starts to be visible and a complete separation of the lower row can be seen at around a distance of x = 2c (airfoil chord, c) from the trailing edge of the airfoil. However, the upper row detaches at around x = 3c that is around a chord distance later than the upper detachment distance. The shapes of the vortices closer to the airfoil change as the wakefield approach toward the downstream direction. The gradient at the trailing edge of the airfoil, and vortices are more dominant. However, from the top views of the vortex patterns, it can be noticed that the flow vortex patterns do not lose their symmetric patterns along the span.

Two separated counter rotating vortices can be seen at α = 8°. The upper vortex row detaches and creates a clockwise rotating vortex at around x = 2.5c distance from the trailing edge of the airfoil. On the other the lower row generates a counterclockwise rotating vortex at almost the same distance from the airfoil. Later, both the upper and the lower rows dissipate without generating any other fully separated vortices. No asymmetric patterns can be observed from the top view of the wakefield on the 3D airfoil along the spanwise direction.

At α = 9°, the upper wakefield row detaches and then merges into the continuous vortex sheet without creating any separated vortex. However, the lower wakefield row detaches, creates a fully developed counterclockwise roating triangular shaped vortex at a distance of x = 2.5c, and then dissipates into the the continuous vortex sheet. From the top view from the right column, no disturbance in symmetric pattern can be seen along with the spanwise direction of the airfoil.

Different figure can be noticed at α = 10° where, both the upper and lower wakefield rows detaches at x = 2c and x = 3c distances from the airfoil, respectively. Then they both generate counter rotating vortices at the top and the bottom of the wake and merge in with the continuous vortex flow sheet. No asymmetric pattern can be seen along the spanwise direction in this case either.

CHAPTER 5

CONCLUSION

Effect of airfoil camber and incidence angle on unsteady aerodynamic behavior around the airfoil at low Reynold number is incestigated in this paper keeping the airfoil thickness constant. Four cambered airfoils (NACA 1412, NACA 2412, NACA 3412, and NACA 4412) are used for the simulations in order to obtain necessary data.

Firstly, numerical simulations of four cambered airfoils: NACA1412, NACA 2412, NACA 3412, and NACA4412 are conducted in the 2D domain for angles of attack 0° to 10° with an increment of 1° per simulation at very low Reynolds number (Re= 1000). Different instantaneous and mean aerodynamic parameters: lift coefficients, drag coefficients, pressure distributions, skin friction coefficients, Strouhal number, and wakefield vortex patterns are discussed and are then demonstrated in the figures. Then the effect of camber is discussed in every parameter to understand the significance of camber on unsteady aerodynamic behavior.

It can be concluded from the different cambered airfoil analyses that the higher cambered airfoils generated higher lift and higher drag force for a specific angle of attack at low Reynolds number. One point should be noted that for 1% increase in camber leads to 7-9% increase in lift and 2.5% increase in drag at the same time. Therefore, this tradeoff should be taken into consider while designing wings of flapping wing MAVs. From the flow separation analyses it can be noticed that as the camber of airfoil increases, the initial flow separation point moves towards the rear side of the airfoil. At the same time, higher camber provides longer flow separation region. These, characteristics can be helpful for delaying flow separation point towards the trailing edge when designing MAV flapping wings.

Instantaneous lift coefficient amplitude spectrul analyses and vortex shedding pattern of different cambered airfoils at different angles of attack indicate that only higher cambered airfoils (NACA 4412) start generating oscillation in the wakefield at relatively low angle of attack ($\alpha = 6°$). Airfoils with lower camber tends to begin generating oscillation at higher angles of attack than $\alpha = 6°$. Both Strouhal number spikes and vortex shedding patterns demonstrate the similar conclusions.

On top of that, a 3D domain is developed and then simulated for NACA 4412 which is the highest lift generating airfoil within those mentioned airfoils at various angles of attack. Then comparisons are discussed in detail between 2D and 3D analyses in terms of aerodynamic parameters to understand whether the airfoil behaves differently in the 3D domain or not.

From the aerodynamic forces study of two-dimensional and three-dimensional simulations over NACA 4412, it can be noted that in terms of global aerodynamic parameters both results are pretty similar for the angle of attack range of 0° to 10°. From pressure distribution, it can be seen that the suction pressure on the upper surface in three-dimensional simulation is a little bit higher than the two-dimensional simulation results. Wakefield vortex patterns in the downstream of both two-dimensional and three-dimensional demonstrate that vortex formation starts at $\alpha = 7°$ but the oscillation in the downsteam wakefield can be seen at $\alpha = 6°$. Instantanous lift coefficient amplitude spectrum indicates the similar results.

As a part of future studies, cambered airfoils can be analysed at high Reynolds number where the aerodynamic parameters can be observed for different cambered airfoils. On top of that, maximum thickness of airfoils can also be investigated for different angles of attack at different Reynolds numbers.

REFERENCES

Abbott, I. H., & von Doenhoff, A. E. (1959). *Theory Of Wing Sections Including a Summary of Airfoil Data*.

Altenbuchner, C., & Hubbar Jr, J. E. (2018). *Modern Flexible Multi-Body Dynamics Modeling Methodology For Flapping Wing Vehicles*.

ANSYS Fluent Users Guide. (n.d.).

Bearman PW. (1966). On vortex street wakes. *A.R.C 28 143*.

Birch, J., & Dickinson, M. (2003). The influence of wing–wake interactions on the productions of aerodynamic forces in flapping flight. *Journal of Experimental Biology*, *206*, 2257–2272. https://doi.org/10.1242/jeb.00381

Bluman, J., & Kang, C. K. (2017). Wing-wake interaction destabilizes hover equilibrium of a flapping insect-scale wing. *Bioinspiration and Biomimetics*, *12*(4). https://doi.org/10.1088/1748-3190/aa7085

Bohorquez, F., Pines, D., & Samuel, P. D. (2010). Small rotor design optimization using blade element momentum theory and hover tests. *Journal of Aircraft*, *47*(1), 268–283. https://doi.org/10.2514/1.45301

Dickinson, M. H., Lehmann, F.-O., & Sane, S. P. (1999). Wing Rotation and the Aerodynamic Basis of Insect Flight. *SCIENCE*, *284*(5422), 1954–1960.

Ellington, C., van den Berg, C., Willmott, A., & Thomas, A. (1996). Leading-edge vortices in insect flight. *NATURE*, *384*, 626–630. https://doi.org/10.1038/384626a0

Gopalakrishnan Meena, M., Nair, A. G., & Taira, K. (2018). Network community-based model reduction for vortical flows. *Physical Review E*, *97*(6). https://doi.org/10.1103/PhysRevE.97.063103

Gopinath, A. K., & Jameson, A. (2006). *Application of the Time Spectral Method to Periodic Unsteady Vortex Shedding*.

Grauer, J., & Hubbard, J. E. (2011). *Modeling and System Identification of an Ornithopter Flight Dynamics Model*.

Huang, R., Wu, J. Y., Jeng, J. H., & Chen, R. C. (2001). Surface flow and vortex shedding of an impulsively started wing. In *J. Fluid Mech* (Vol. 441).

Kang, C., Fahimi, F., Griffin, R., Landrum, D. B., Mesmer, B., Zhang, G., Lee, T., & Aono, H. (2018). *Marsbee- Swarm of flapping wing flyers for enhanced MARS exploration*.

Kang, C. K., & Shyy, W. (2013). Scaling law and enhancement of lift generation of an insect-size hovering flexible wing. *Journal of the Royal Society Interface*, *10*(85). https://doi.org/10.1098/rsif.2013.0361

Kouser, T., Xiong, Y., Yang, D., & Peng, S. (2021). Direct Numerical Simulations on the three-dimensional wake transition of flows over NACA0012 airfoil at Re = 1000. *International Journal of Micro Air Vehicles*, *13*. https://doi.org/10.1177/17568293211055656

Kunz, P. J. (2003). *Aerodynamics And Design for Ultra-Low Reynolds Number Flight*.

Kunz, P., & Kroo, I. (2000). Analysis and Design of Airfoils for Use at Ultra-Low Reynolds Numbers. In *Fixed and Flapping Wing Aerodynamics for Micro Air Vehicle Applications* (pp. 35–60). American Institute of Aeronautics and Astronautics. https://doi.org/10.2514/5.9781600866654.0035.0060

Kurtulus, D. F. (2015). On the unsteady behavior of the flow around NACA 0012 airfoil with steady external conditions at Re=1000. *International Journal of Micro Air Vehicles*, *7*(3), 301–326. https://doi.org/10.1260/1756-8293.7.3.301

Kurtulus, D. F. (2016). On the wake pattern of symmetric airfoils for different incidence angles at Re=1000. *International Journal of Micro Air Vehicles*, *8*(2), 109–139. https://doi.org/10.1177/1756829316653700

Mateescu, D., & Abdo, M. (2010). Analysis of flows past airfoils at very low Reynolds numbers. *Proceedings of the Institution of Mechanical Engineers, Part G: Journal of Aerospace Engineering*, *224*(7), 757–775. https://doi.org/10.1243/09544100JAERO715

McMasters, J. H., & Henderson, M. J. (1980). Low speed single element airfoil synthesis. *Technical Soaring*, *6*, 1–21.

NASA Langley. (2014). *NASA Langley*. https://images.nasa.gov

Norberg, U. M. (1990). Vertebrate flight: Mechanics, physiology, morphology, ecology and evolution. *Springer-Verlag*.

Ohmi, K., Coutanceau, M., Phuoc Loc, T., & Dulieu, A. (n.d.). *Vortex formation around an oscillating and translating airfoil at large incidences By Kazuo Ohmi', Madeleine Coutanceau2, Ta Phuoc Loc3 A N D A N N I E Dulieu3*.

Ol, M. v, Mcauliffe, B. R., Hanff, E. S., Scholz, U., & Kähler, C. (2009). *Comparison of Laminar Separation Bubble Measurements on a Low Reynolds Number Airfoil in Three Facilities*.

Platzer, M. F., & Jones, K. D. (2006). *Flapping Wing Aerodynamics-Progress and Challenges*.

Roshko A. (1954). On the drag and shedding Frequency of two dimensional bluff bodies. *NACA Technical Note 3169*.

Sane, S., & Dickinson, M. (2002). The aerodynamic effects of wing rotation and a revised quasi-steady model of flapping flight. *Journal of Experiemental Biology*, *205*, 1087–1096.

Schaefer, J., & Eskinazi, S. (1959). An analysis of the vortex street generated in a viscous fluid. *J Fluid Mech*.

Shyy, W. (Wei). (2008). *Aerodynamics of low Reynolds number flyers*. Cambridge University Press.

Shyy, W. (Wei), Aono, H., Kang, C., & Liu, H. (2013). *An introduction to flapping wing aerodynamics*.

Strykowski, P., & Sreenivasan, K. (1990). On the formation and suppression of vortex '"shedding"' at low Reynolds numbers. *J Fluid Mech*.

Suzuki T., J. H., & Yamamoto, F. (2009). Unsteady PTV velocity field past an airfoil solved with DNS: Part 1. Algorithm of hybrid simulation and hybrid velocity field at Re = 1000. *Exp Fluids*, *47*, 957–976.

Suzuki, T., Sanse, A., Mizushima, T., & Yamamoto, F. (2009). Unsteady PTV velocity field past an airfoil solved with DNS: Part 2. Validation and application at Reynolds numbers up to Re = 10000. *Exp Fluids*, *47*, 977–994.

Taylor, K. G., Nudds, R. L., & Thomas, A. L. R. (2003). Flying and Swimming animals cruise at a Strouhal number tuned for high power efficiency. *Nature*, *425*(6959), 705–707. https://doi.org/10.1038/nature02047

Thomas, M., & Boyer, M. (2011, February 17). *Aerovironment Develops World's F First Fully Operational Life-Size Hummingbird-like Unmanned Aircraft for DARPA.* AeroVironment, Inc. https://www.avinc.com/resources/press-releases/view/aerovironment_develops_worlds_first_fully_operational_life-size_hummingbird

Unsplash. (2021). *Unsplash*. https://unsplash.com/

Weis-Fogh, T. (1973). Quick estimates of flight fitness in hovering animals, including novel mechanism for lift production. *Journal of Experimental Biology*, 169–230.

Yang, L.-J., & Esakki, B. (2021). *Flapping Wing Vehicles; Numerical and Experimental Approach*.

Yang, W., Wang, L., & Song, B. (2018). Dove: A biomimetic flapping-wing micro air vehicle. *International Journal of Micro Air Vehicles*, *10*(1), 70–84. https://doi.org/10.1177/1756829317734837

Zdravkovich MM. (1996). Different Modes of vortex shedding: an overview. *J Fluid Struct*.